Single-grain feldspar luminescence chronology of historical extreme wave event deposits recorded in a coastal lowland, Pacific coast of central Japan

Riedesel, Svenja; Brill, Dominik; Roberts, H. M.; Duller, Geoffrey; Garrett, Edward; Zander, Anja; King, Georgina; Tamura, Toru; Burow, Christoph; Cunningham, Alasdair; Seeliger, Martin; De Batist, Marc; Heyvaert, Vanessa M. A.; Fujiwara, Helmut; Brückner, Helmut; QRN Team

Published in:
Quaternary Geochronology

DOI:
10.1016/j.quageo.2018.01.006

Publication date:
2018

Citation for published version (APA):
Riedesel, S., Brill, D., Roberts, H. M., Duller, G., Garrett, E., Zander, A., King, G., Tamura, T., Burow, C., Cunningham, A., Seeliger, M., De Batist, M., Heyvaert, V. M. A., Fujiwara, H., Brückner, H., & QRN Team (2018). Single-grain feldspar luminescence chronology of historical extreme wave event deposits recorded in a coastal lowland, Pacific coast of central Japan. *Quaternary Geochronology*, *45*, 37-49. https://doi.org/10.1016/j.quageo.2018.01.006

Single-grain feldspar luminescence chronology of historical extreme wave event deposits recorded in a coastal lowland, Pacific coast of central Japan

Svenja Riedesel[1,2*], Dominik Brill[1], Helen M. Roberts[2], Geoff A. T. Duller[2], Ed Garrett[3,4], Anja M. Zander[1], Georgina E. King[5], Toru Tamura[6], Christoph Burow[1], Alastair Cunningham[7,8], Martin Seeliger[1], Marc DeBatist[9], Vanessa M. A. Heyvaert[4], Osamu Fujiwara[6], Helmut Brückner[1] and the QuakeRecNankai team[10]

[1] *Institute of Geography, University of Cologne, Germany*

[2] *Department of Geography and Earth Sciences, Aberystwyth University, United Kingdom*

[3] *Department of Geography, Durham University, United Kingdom*

[4] *Geological Survey of Belgium, Brussels, Belgium*

[5] *Institute of Geological Sciences and Oeschger Centre for Climate Change Research, University of Bern, Switzerland*

[6] *Geological Survey of Japan, AIST, Japan*

[7] *Department of Geoscience, Aarhus University, DTU Nutech, Risø Campus, DK-4000 Roskilde, Denmark*

[8] *Center for Nuclear Technologies, Technical University of Denmark, DTU Risø Campus, DK-4000 Roskilde, Denmark*

[9] *Department of Geology, Ghent University, Belgium*

[10] *List of members available from http://www.quakerecnankai.ugent.be/index.php?team*

* Corresponding author:

riedeselsvenja@gmail.com, svr1@aber.ac.uk

Present address:

Department of Geography and Earth Sciences,

Aberystwyth University,

Aberystwyth SY23 3DB

United Kingdom

Abstract

The Shirasuka lowlands, located on the Enshu-nada coast of central Japan, record evidence for numerous extreme wave events. Here we test the applicability of using the luminescence signal from feldspars to date these young (< 1000 a) extreme wave event deposits. The signal used for dating is the IRSL signal (measured at 50°C) as part of a post-IR $IRSL_{130}$ procedure. We demonstrate that this $IRSL_{50}$ (pre-IR_{130}) signal results in reliable ages when corrected for fading, and the post-IR $IRSL_{130}$ stimulation functions as an optical wash for both the natural/regenerated luminescence signal (L_x) and the test dose signal (T_x), lowering the recuperation and removing any remaining charge from previous steps in the protocol. The single grain $IRSL_{50}$ (pre-IR_{130}) ages generated, cover the historical record of the past 800 years and correlate well with past earthquakes and tsunamis in AD 1361, AD 1498 and AD 1605. Another identified tsunami deposit may correlate with the AD 1707 earthquake and tsunami. A slope failure deposit, probably caused by the earthquake in AD 1944, is also identified. This study demonstrates that accurate ages can be determined for the young, extreme wave events at this site using the luminescence signal from feldspars.

Keywords

Feldspar; single-grain dating; $IRSL_{50}$; low temperature post-IR IRSL; tsunami

1 Introduction

The Indian Ocean Tsunami in 2004 and the Tōhoku-oki Tsunami in 2011 caused dramatic damage to coastal settlements and thousands of casualties, drawing the attention of the public and scientists to the impact and history of tsunamis. Since then, numerous studies

have developed approaches to identify the characteristics, impact and age of tsunami deposits (e.g. Dawson & Stewart, 2007; Jankaew et al., 2008; Monecke et al., 2008; Engel et al., 2010; Switzer et al., 2012; May et al., 2016). Storm surges, another major threat to coastal communities, are also the focus of research due to recent disasters like Typhoon Haiyan, which hit the Philippine coast in 2013 (e.g. Brill et al., 2016; Pilarczyk et al., 2016; Soria et al., 2017). Studies observing proxies and characteristics of extreme wave event deposits contribute to improvements in their identification in the geological record (e.g. Morton et al., 2007; Chagué-Goff et al., 2011; Shanmugam, 2012), while chronological studies of past extreme wave events enable the identification of recurrence intervals, intensities and past impacts (Brill et al., 2012a; Prendergast et al., 2012).

The Shirasuka lowlands in central Japan record evidence for numerous extreme wave events, as previously demonstrated by Fujiwara et al. (2006), Komatsubara et al. (2008) and Garrett et al. (accepted). The sedimentary record of extreme wave event deposits of the Shirasuka lowlands has been constrained by radiocarbon dating to be younger than AD 1200 (Fujiwara et al., 2006; Komatsubara et al., 2008). From 12th century AD onwards, at least six megathrust earthquakes and subsequent tsunamis occurred in the eastern segments (C and D) of the Nankai Trough (Ando, 1975; Fig. 1). The region also has a long historical record of earthquakes and subsequent tsunamis from AD 684 onwards, captured in a range of sources such as chronicles (e.g. *Nihon Shoki*), reports, and governmental records (e.g. Ando, 1975; Usami, 1979; Ishibashi, 2004; Goff et al., 2016). However, there are several issues which have complicated previous efforts to reconstruct the local record of past extreme wave events based on the study of the sedimentary evidence preserved at Shirasuka: (1) The lowlands provide a complex stratigraphy with laterally discontinuous event layers, which com-

plicates stratigraphic correlations between sediment cores (Fujiwara et al., 2006; Komatsubara et al., 2008; Garrett et al., accepted), and makes chronology essential to correlate different core records; (2) the lack of material appropriate for radiocarbon dating often means that this method cannot always be used to determine ages where they are needed; (3) even where material suitable for radiocarbon dating exists, a plateau in the radiocarbon calibration curve prevents the establishment of a high-resolution chronostratigraphy during the time period of interest (Stuiver, 1978; Madsen et al. 2009).

Unlike radiocarbon dating, optically stimulated luminescence (OSL) techniques do not typically suffer from a lack of suitable material for dating as they rely upon use of one of the two most abundant minerals on Earth, quartz or feldspars. A further advantage of OSL is that the sediments used for dating directly record the age of the deposition event, e.g. the burial age of a tsunami event layer (e.g. Brill et al., 2012a, b). However, whilst the use of OSL has previously been explored in a range of extreme wave event settings (Huntley & Clague, 1996; Murari et al., 2007; Cunha et al., 2010; Brill et al., 2012a, b; Prendergast et al., 2012; Spiske et al., 2013; Tamura et al., 2015), issues still persist. Firstly, incomplete resetting of the luminescence signal during tsunami or storm surge transport, prior to deposition of the sediments, needs to be considered (e.g. Madsen & Murray, 2009). The fast component of the OSL signal from quartz bleaches more rapidly than any other luminescence signal routinely used for dating, and this makes it the preferred mineral for dating young and potentially incompletely-bleached sediments (e.g. Bishop et al., 2005; Murari et al., 2007; Cunningham et al., 2011; Brill et al., 2012a, b; Li et al., 2017). However, previous studies of quartz OSL in tectonically active regions have shown challenging luminescence properties (e.g. Tsukamoto et al., 2003; Kondo et al., 2007; Steffen et al., 2009; Neudorf et al., 2015; Tamura et al.,

100 2015). Thus, OSL of feldspars may provide a useful alternative chronometer if they can be
101 demonstrated to be suitable for dating very young (< 1000 years), and potentially incom-
102 pletely-bleached sediments.
103
104 The OSL signal from feldspar bleaches more slowly than that of quartz (e.g. Buylaert et al.,
105 2012; Colarossi et al., 2015), and suffers from an athermal signal loss called anomalous fad-
106 ing (Wintle, 1973), which can result in age under-estimations. Low-temperature post-
107 infrared infrared stimulated luminescence (post-IR IRSL) dating offers a promising approach
108 for dating young deposits using feldspars (e.g. Madsen et al., 2011; Reimann & Tsukamoto,
109 2012), since it may minimise anomalous fading whilst still accessing signals that are ade-
110 quately bleached for dating (Kars et al., 2014). However, it should be noted that previous
111 applications were to dune and beach deposits, where the opportunity for exposure to day-
112 light prior to deposition is much greater than may be the case for high magnitude events
113 such as a tsunami.
114
115 In this study we aim to test the suitability of optically stimulated luminescence (OSL) tech-
116 niques to provide a chronology for young (< 1000 years) extreme wave event deposits in the
117 Shirasuka lowlands of tectonically active central Japan. If successful, OSL may help refine the
118 record of extreme wave events preserved at both Shirasuka and elsewhere.
119
120 **2 Field site**
121 **2.1 Study area and existing chronostratigraphy**
122 The Japanese islands are situated at two triple junctions of tectonic plates. South of the main
123 island of Honshu, the Philippine Sea Plate subducts beneath the Eurasian Plate at a rate of

approximately 40–55 mm/a (Mazzotti et al., 2000; Loveless & Meade, 2010). The subduction zone is subdivided into six segments (Fig. 1a), which have ruptured during twelve historically documented multi-segment megathrust earthquakes (> M8) since AD 684 (Ando, 1975; Satake, 2015; Garrett et al., 2016). The study area of Shirasuka (Fig. 1b) is located close to the approximate boundary of segments D and E (Fig. 1a).

Sandwiched between a ~60–80 m high mid-Pleistocene terrace and a ~10 m high coastal dune (height artificially increased in the early 21st century, because of the construction of the Shiomi By-pass of Japan National Route 1), the marshy coastal lowlands of Shirasuka are ideally situated to record evidence of typhoons and tsunamis (Fig. 1b). Sediment cores from the lowlands are mainly composed of fine-grained marsh deposits intercalated with sand-rich layers (Fujiwara et al., 2006; Komatsubara et al., 2008; Garrett et al., accepted; Fig. 2). Komatsubara et al. (2008) obtained a set of cores (hexagonal symbols on Fig. 1b) from these lowlands and used 21 radiocarbon ages to generate a chronology for them which covers the timespan from ~AD 1200 onwards. The cores include sand layers interpreted as resulting from tsunamis and storm surges as well as slope failures (event deposits A to G in ascending order, according to Komatsubara et al., 2008). Komatsubara et al. (2008) tentatively correlate the sand layers B, C, E and F in their cores with the AD 1498 Meiō, 1605 Keichō, 1707 Hōei and AD 1854 Ansei-Tōnankai events where both an earthquake and a tsunami are recorded. Given the excellent historical record of extreme wave events available for this region, this study site provides an ideal opportunity to assess whether luminescence dating can provide accurate ages for extreme wave events.

2.2 Fieldwork and sampling strategy

Two overlapping sediment cores taken ~0.5 m apart (JSH1b/full, JSH1/overlap; Figs. 1, 2) were recovered by vibra coring (Atlas Copco Cobra TT) using closed steel auger heads and opaque 50 mm diameter PVC tubes. Sediment cores were opened in the laboratory under subdued red light. The sediment cores consist of clayey-silty deposits with intercalated sand layers. The lower contact of the sand layers is aprupt and the sand includes clay lenses (rip-up clasts) and mud caps. This suggests rapid high-energy erosional processes. We interpret the sand layers to be either tsunami or storm surge deposits. The stratigraphy for both sediment cores is shown in Fig. 2 and described in detail in Garrett et al. (accepted). Sand layers were sampled for luminescence dating and dosimetry. Where the stratigraphy changed within 30 cm of an OSL sample, additional dosimetry samples were taken from the differing sedimentary units within 30 cm distance from the OSL sample, to adequately assess the dose rate to that OSL sample. In total, 10 samples were dated by OSL (Fig. 2), the dose rate was determined for 18 samples (Fig. 2; Table S1). In addition, two modern samples (Fig. 1b) were collected from the beach by hammering opaque plastic tubes in the sand, approximately 2-3 cm below the surface.

3 Luminescence dating

3.1 Sample preparation

Luminescence samples were prepared under subdued red light in the Cologne Luminescence Laboratory (CLL). Prior to palaeodose determination, hydrochloric acid (HCl; 10 %), hydrogen peroxide (H_2O_2; 10 %) and sodium oxalate ($Na_2C_2O_4$; 0.01 N) were used to remove carbonates, organic matter and to disperse the particles. Samples were dry sieved to separate the 100–200 µm fraction that was then density separated using sodium polytungstate to isolate quartz (2.68 g/cm^3 > ρ > 2.62 g/cm^3) and alkali-feldspar fractions (ρ < 2.58 g/cm^3). The

quartz fraction was etched with concentrated hydrofluoric acid (40 %) for 40 min and subsequently treated with HCl (10 %) to remove any fluorides. Subsequent tests of the quartz material suggested that, in accordance with other studies on Japanese quartz (e.g. Tsukamoto et al., 2003; Tamura et al., 2015), the material shows inappropriate luminescence properties, which are unsuitable for quartz OSL dating. Hence, quartz is not considered further in the manuscript, although the main characteristics are outlined in Supplementary Information.

Multiple grain (MG) measurements were made at the CLL, using grains mounted on stainless steel discs and fixed using a 1 mm patch of silicone oil. Single-grain (SG) measurements were made at the Aberystwyth Luminescence Research Laboratory (ALRL), using 100–200 µm grains brushed into the 300 µm diameter holes of standard single-grain discs. The size-range of the sieved fraction may cause the presence of more than one grain within one hole; this was checked on a random basis and was found to occur only very occasionally.

3.2 Dosimetry

Uranium (U), Thorium (Th) and Potassium (K) contents were determined by high-resolution gamma spectrometry in the CLL. Approximately 200 g of dried, homogenised sediment was stored in an airtight box for at least four weeks to compensate for radon loss induced by sample preparation, before measurement with an Ortec Profile M-Series GEM Coaxial P-type high-precision Germanium Gamma-Ray detector. For eight samples (JSH1-2Dn, JSH1-6Dn-7Dn, JSH1-10Dn, and JSH1-16Dn to JSH1-20Dn), only very small amounts of sediment were available; these were measured at VKTA Dresden using low-level-gamma spectrometry (Table S1).

To measure the potassium content of the alkali-feldspar separates, 100 mg of each sample was analysed on a Risø GM-25-5 beta counter. An average internal K-content of 6.44 ± 1.05 % was measured (Table 1) but a K-content of 10 ± 2 % was used to calculate the dose rate used in combination with equivalent doses (D_e) from single grains, assuming that the grains with higher K-content have a brighter IRSL signal and are more likely to generate a D_e (Smedley et al., 2012).

The stratigraphy of the Shirasuka lowlands is complex and shows abrupt changes in grain size, which may cause variations in the gamma dose rate. Layer-to-layer variations in gamma dose rate were calculated according to Aitken (1985, Appendix H), using the multi-layer gamma spreadsheet of Ian Bailiff, Durham University (personal communication) to give the gamma dose rate values shown in Table 1. DRAC v1.1 (Durcan et al., 2015) was used to calculate internal and external alpha and beta dose rates, and to correct them for water content. Conversion factors for gamma and beta dose rates are based on Adamiec & Aitken (1998). Alpha and beta grain size attenuation factors of Bell (1980) and Guerin et al. (2012, for feldspars), respectively, were applied. Alpha efficiency was determined for samples JSH1-4 and JSH1-10, and gave values of 0.072 ± 0.003 for the $IRSL_{50}$ (pre-IR_{130}) signal, and 0.095 ± 0.008 for the post-IR $IRSL_{130}$ signal (see Supplementary Information for further details). The cosmic dose rate was determined in accordance with Precott and Hutton (1994). Information on dose rates (Gy/ka) calculated for each sample in this study are given in Table 1.

3.3 Instrumentation and methods for feldspar measurements

Luminescence measurements were made using single-aliquot regenerative dose (SAR) protocols on Risø TL/OSL readers equipped with $^{90}Sr/^{90}Y$ beta sources delivering dose rates of ~0.0837 Gy/s, ~0.0760 Gy/s and ~0.0366 Gy/s, depending on the instrument.

Two sets of OSL measurements were made on feldspars. Small (1 mm diameter), multiple-grain aliquots were measured at the CLL, stimulated using IR LEDs (870 nm, FWHM 40 nm) and detected through a D410/30x LOT interference filter. Single-grain equivalent dose measurements were performed at ALRL using an IR laser (830 nm, 150 mW, with a Schott RG-780 filter in front of the laser to remove emission below 780 nm) and detected using a combination of 4.1 mm BG-39 and 2.1 mm Corning 7-59 glass filters. A convex quartz lens was used to maximise the signal collection efficiency during single grain measurements.

All feldspar single-aliquot and single-grain datasets with recycling ratios and test dose uncertainties within 10 % were accepted for palaeodose calculations (see section 4 for details of the measurement protocols considered). Fading measurements were conducted according to Auclair et al. (2003). The samples were bleached for 24 hours in a Hönle SOL 2 solar simulator and subsequently irradiated to ~23 Gy. The shortest delay between the start of an irradiation and the start of a measurement was 218 s, the longest 18,000 s. Ages were corrected for fading using the correction model of Huntley & Lamothe (2001) implemented in the R-package 'Luminescence' (Kreutzer et al., 2012; Kreutzer et al., 2016).

4 Measurement protocols for feldspar

Inappropriate luminescence properties of the quartz in this study means that reliable signals cannot be obtained for quartz OSL dating (see Supplementary Information). Measurement

243 protocols using infra-red stimulated luminescence (IRSL) signals from feldspar were there-
244 fore investigated, using multiple-grain aliquots of coarse-grain feldspar to examine the signal
245 behaviour and identify the most appropriate measurement conditions, prior to D_e determi-
246 nation using single-grains (section 5). Two different approaches were tested. First, an $IRSL_{50}$
247 SAR protocol (Wallinga et al., 2000) was investigated, because whilst the signal does not
248 bleach as quickly as quartz, it does still bleach relatively quickly compared to many other
249 feldspar signals obtained using higher stimulation temperatures (e.g. Buylaert et al., 2012;
250 Colarossi et al., 2015). Secondly, a low-temperature post-IR IRSL protocol (Madsen et al.,
251 2011; Reimann & Tsukamoto, 2012) was investigated. This protocol yields both an $IRSL_{50}$
252 signal, and a post-IR IRSL signal, which is likely to have a lower rate of anomalous fading than
253 the $IRSL_{50}$ signal but a slower bleaching rate (e.g. Buylaert et al., 2012; Colarossi et al., 2015).
254
255 The impact of including a high-temperature clean-out step (Murray & Wintle, 2003) at the
256 end of each post-IR IRSL measurement cycle (e.g. Thiel et al., 2011; Buylaert et al., 2012) was
257 explored for the post-IR IRSL measurement procedure by stimulating with IR for 100 s while
258 holding the sample at a temperature of 180 °C following each test dose measurement. Alt-
259 hough this clean-out step is designed to remove any remaining signal at the end of each SAR
260 cycle, it made difference to our D_e or to our recuperation values measured from multiple-
261 grain aliquots using both the $IRSL_{50}$ (pre-IR_{130}) and the post-IR $IRSL_{130}$ signal. For this reason,
262 and to avoid the potential of introducing further sensitivity change, a high-temperature
263 clean-out step was not included in the measurement sequences used to generate any of the
264 data considered in this study.
265

The suitability of the $IRSL_{50}$ and post-IR IRSL protocols was tested with preheat, preheat dose-recovery (all dose-recovery data in this study is reported after subtracting the residual dose measured from grains that had been bleached for 24 hours by the solar simulator), and residual dose preheat plateau tests, applied to sample JSH1-6.

4.1 Tests of the $IRSL_{50}$ protocol

The effect of preheat temperature was investigated for the first approach, the $IRSL_{50}$ protocol shown in Table 2a. Three aliquots were measured at each preheat temperature. Preheat temperatures ranged from 190 °C to 290 °C and were held for 10 s. For all measurements, the test dose signal (Tx) preheat conditions are the same as the preheat conditions of the natural and regenerative dose signal (Lx) (Blair et al. 2005).

The preheat plateau (Fig. 3a) shows no dependence of $IRSL_{50}$ D_e upon thermal pretreatment, in accordance with the findings of Murray et al. (2009). Recuperation (expressed in Gy) increases with increasing preheat temperature (Fig 3b), with the lowest value (0.11 ± 0.01 Gy, n = 3) being observed following a preheat at 190 °C. The lowest tested preheat temperature of 190 °C was chosen for further analyses in order to minimise recuperation and hence facilitate measurement of low natural doses. The suitability of this preheat temperature was validated with a dose-recovery test: six aliquots were bleached for 24 hours in a Hönle SOL2 solar simulator, three of which were measured for dose-recovery (given dose: ~1.7 Gy) and the remaining three the residual dose.

A typical decay curve and dose-response curve for this $IRSL_{50}$ (preheat 190 °C) signal is shown in Figure 3c. Data generated using this $IRSL_{50}$ (preheat 190 °C) protocol passed all per-

formance tests (recycling ratio, test dose error, and dose-recovery test within 10 % uncertainties), and the residual dose remaining after 24 hours of bleaching in the SOL2 solar simulator was determined to be 0.20 ± 0.01 Gy (n=3). The fading rate of the $IRSL_{50}$ (preheat 190 °C) signal was determined to be of 2.9 ± 1.3 %/decade for sample JSH1-6.

4.2 Tests of the post-IR IRSL protocol

For the second approach, tests on the suitability of different temperatures in the post-IR IRSL protocol (Table 2b) followed the same procedure as described in section 4.1 for the $IRSL_{50}$ signal. All post-IR IRSL measurements were preceded by an IRSL measurement at 50 ^{o}C, irrespective of preheat conditions. Preheat temperatures were tested in a range from 120 °C up to 240 °C, in steps of 20°C, plus an additional temperature of 255 °C (selected so that the post-IR $IRSL_{225}$ signal that has been widely studied previously could be measured). All preheats were held for 10 s and were followed by post-IR IRSL measurements made at elevated temperatures that tracked the preheat temperature by -30 °C (termed the post-IR $IRSL_{elev}$ signal). The duration of the preheat was chosen based on the protocol proposed by Madsen et al. (2011) for young samples. We checked for any isothermal thermoluminescence contribution to our IRSL signals by measuring the signal with no optical stimulation for 5 channels before optical stimulation started. No isothermal signal was found. For all measurements, the natural or regenerative dose signal (L_x) and test dose signal (T_x) preheat conditions are the same as each other.

For each preheat temperature examined, six aliquots were bleached for 24 hours in a Hönle SOL2 solar simulator. Three of these were used for a dose-recovery test (given dose: ~2.0 Gy) and the remaining three aliquots were used for measuring the residual dose.

314

315 **4.2.1 $IRSL_{50}$ (pre-IR_{elev}) signal**

316 The $IRSL_{50}$ (pre-IR_{elev}) signal shows no dependence of equivalent dose on preheat tempera-
317 ture (Fig. 4a), other than the size of the uncertainties on each equivalent dose determination
318 typically increasing with increasing preheat temperature. The dose-recovery tests conducted
319 at different temperatures suggest that the $IRSL_{50}$ (pre-IR_{elev}) signal can recover a dose within
320 1σ uncertainties for preheat temperatures of up to 160 °C (Fig 4d). For preheat tempera-
321 tures ≥ 180 °C (Fig. 4c), the residual dose measured following 24 hours of bleaching in the
322 SOL2 solar simulator increases with increasing preheat temperature. Taking the signal inten-
323 sity, relative bleachability of signals (inferred from the residual dose values), recuperation
324 and dose recovery test data into account (Figs. 4a-e), the $IRSL_{50}$ (pre-IR_{130}) protocol was
325 identified as being suitable for further consideration in this study.

326

327 Is there any difference between data obtained using the $IRSL_{50}$ signal (protocol given in Table
328 2a) and the $IRSL_{50}$ (pre-IR_{130}) signal (protocol given in Table 2b) that might make one more
329 suitable for dating than the other? Despite different preheat temperatures (i.e. 190 °C for
330 the $IRSL_{50}$ protocol compared to 160 °C for the $IRSL_{50}$ (pre-IR_{130}) signal), the $IRSL_{50}$ lumines-
331 cence signals measured within the post-IR $IRSL_{130}$ protocol are similar to the signals of the
332 $IRSL_{50}$ protocol. Both signals are bright (1 mm aliquots yield several thousand counts per
333 0.8 s, e.g. Figs. 3c and 4e), and fading is identical within uncertainties (g_{2days} values of
334 2.92 ± 1.26 [n = 3, sample JSH1-6] and 3.24 ± 1.26 %/decade [n = 3, JSH1-10] were measured
335 for the $IRSL_{50}$ signal of two samples, and values for the $IRSL_{50}$ (pre-IR_{130}) signal varied be-
336 tween 1.84 ± 1.23 %/decade [n = 3, JSH1-13] to 3.17 ± 1.26 %/decade [n = 3, JSH1-10]). A
337 mean of g_{2days} 2.48 ± 0.52 %/decade was measured for the $IRSL_{50}$ (pre-IR_{130}) signal of all ex-

amined samples (n = 10). Measured residuals after 24 hours of bleaching in a SOL2 are 0.20 ± 0.01 Gy and 0.12 ± 0.04 Gy, for the $IRSL_{50}$ and $IRSL_{50}$ (pre-IR_{130}) signal, respectively, both measured on sample JSH1-6. These results indicate further resetting of the signal when using the $IRSL_{50}$ (pre-IR_{130}). The recuperation of the $IRSL_{50}$ (pre-IR_{130}) signal (0.01 ± 0.00 Gy, n = 3, Fig. 4b) is lower than the recuperation of the $IRSL_{50}$ signal (0.11 ± 0.01 Gy, n=3, Fig. 3b). In terms of age, this large difference in recuperation is equivalent to ~3 versus 30 years for the $IRSL_{50}$ (pre-IR_{130}) and $IRSL_{50}$ signals respectively, and could be significant for the samples in this study, where young, high-precision ages are required to test against the historical evidence for extreme wave events. Based on this evidence, the $IRSL_{50}$ (pre-IR_{130}) signal from the post-IR IRSL protocol (Table 2b) seems the most appropriate, but do the post-IR $IRSL_{elev}$ signals offer any advantage?

4.2.2 Post-IR $IRSL_{elev}$ signal

Over the range of preheat and post-IR IRSL stimulation temperatures tested, the post-IR IRSL signal intensity (Fig. 4j) is consistently an order of magnitude lower than either the $IRSL_{50}$ signal reported in section 4.1 (Fig. 3c), or the $IRSL_{50}$ (pre-IR_{elev}) signal measured as part of the post-IR IRSL protocol (section 4.2.1, Fig. 4e). Dose-recovery ratios (DRR) obtained using the post-IR $IRSL_{elev}$ signal are within 10 % of unity (1σ uncertainty) for all preheat temperatures up to 220 °C (except for 200 °C; Fig. 4i). The residual dose remaining following 24 hours of bleaching with the SOL2 solar simulator shows a steady increase with increasing temperature, rising from 0 Gy to 2.33 Gy for the post-IR $IRSL_{elev}$ signal (Fig. 4h).

The influence of charge carry-over on both signals, $IRSL_{50}$ (pre-IR_{130}) and post-IR $IRSL_{130}$, was observed by investigating changes in test dose sensitivity (Fig. 5). Larger variations in T_x/T_n of the post-IR $IRSL_{130}$ compared to the $IRSL_{50}$ (pre-IR_{130}) indicate a source of large recuperation

362 in the post-IR $IRSL_{130}$ signal by carried-over charge, similar to that described by Colarossi et
363 al. (in press). Whilst this charge carry-over is significant for the post-IR $IRSL_{130}$, this second
364 optical treatment (post-IR $IRSL_{elev}$) functions as an optical wash that removes any remaining
365 charge from the $IRSL_{50}$ (pre-IR_{130}) signal. Particularly when dealing with very young samples,
366 it is desirable to minimise thermal transfer in order to obtain more precise ages.
367
368 **4.3 Selecting a protocol for equivalent dose determination**
369 Based on the evidence described above, the post-IR $IRSL_{elev}$ signals are less appropriate for
370 dating these young sediments than the $IRSL_{50}$ (pre-IR_{130}) signal, and so this latter signal was
371 selected for equivalent dose determination. This decision is primarily based on the im-
372 portance of minimising any residual signals or recuperation and was confirmed by meas-
373 urements made on two samples collected from the current beach (JSH-MOD3 and and JSH-
374 MOD4).
375
376 Multiple grain measurements yield unlogged central age model D_e values of 0.14 ± 0.00 Gy
377 for JSH-MOD3 (wet beach sample) and 0.23 ± 0.04 Gy for JSH-MOD4 (dry beach sample) us-
378 ing the $IRSL_{50}$ (pre-IR_{130}) signal. In contrast much higher values are seen using the post-IR
379 $IRSL_{130}$ signal (0.8 ± 0.02 Gy, wet beach sample; 1.28 ± 0.21 Gy, dry beach sample). These
380 results are in agreement with the residual dose values measured following 24 hours of
381 bleaching within the SOL2 (for sample JSH1-6, Figs. 4c and 4h), and supports the decision to
382 use the $IRSL_{50}$ (pre-IR_{130}) signal for dating.
383
384 **5 Single-grain analysis**

385 Samples from the current beach (JSH1-MOD3 and MOD4) give multiple grain D_e values that
386 are not zero, even though they were thought to have been exposed to daylight during the
387 years preceding collection. Additionally, the sediment samples in this study are believed to
388 be derived from energetic tsunami or storm activity where exposure to daylight will be very
389 limited during the final stage of erosion and deposition. Therefore, D_e determination using
390 single-grains of feldspar was investigated so that heterogeneity of bleaching could be stud-
391 ied. The suitability of the measurement protocol was assessed by undertaking a dose recov-
392 ery test, and single grain dose distributions were measured for all samples. Analysis of the
393 shape of the D_e distributions was then undertaken in order to decide which age model
394 should be used for age calculation.
395
396 **5.1 Single grain dose recovery tests**
397 Dose recovery experiments using single-grain measurements were undertaken on three
398 samples (JSH1-4, -6 and -10). The post-IR $IRSL_{130}$ protocol described in Table 2c was used,
399 and data for the $IRSL_{50}$ (pre-IR_{130}) signal used for analysis. Grains were bleached in the SOL2
400 solar simulator for 24 hours prior to analysis. Two or three single grain discs had their D_e
401 measured without any additional dose, and two or three discs received a known laboratory
402 dose of 1.098 Gy. After screening, between 101 and 163 D_e values were obtained (Fig S-2).
403 After subtraction of the dose measured in the grains that received no laboratory dose, the
404 dose recovery ratios were 0.95 ± 0.02, 0.94 ± 0.02 and 0.96 ± 0.04, well within the standard
405 acceptance criteria of 1.00 ± 0.10. This dose recovery experiment shows that the protocol
406 used for these $IRSL_{50}$ (pre-IR_{130}) measurements (Table 2c) is effective at recovering a known
407 laboratory dose. In all cases the dose recovery data were overdispersed (JSH1-4: 10.2%;

JSH1-6: 11.7%; JSH1-10: 18.6%), similar to the value of 16.5% overdispersion observed by Reimann et al. (2012) when measuring a sample that had received a known gamma dose.

5.2 Single grain D_e distributions

The same protocol used for the dose recovery test was then used for single grain measurements of the two samples collected from the current beach adjacent to the core site (Fig. 1b) and the ten samples collected from the two cores (Fig. 2). Examples of the dose distributions arising from these measurements are shown in Fig. 6, and data summarised in Table 3. All single grain equivalent dose distributions are provided in the supplementary material (Fig. S-3 and Fig. S-4).

For the natural signals measured, the D_e distributions are generally unimodal (e.g. Fig. 6a), but increase in width (e.g. Fig. 6b) with increasing depth down-core. In addition, for some of the samples, there are a small number of grains which give slightly larger D_e values compared to the overall distribution (e.g. Fig. 6c) and two samples (JSH1-2 and JSH1-20) where the range of D_e values is much greater (Fig. 6d) and where D_e values of many tens of Gray are found (e.g. JSH1-2 and JSH1-20; Fig. 6d). This may result from incomplete bleaching at deposition, but it is unclear whether this is also the explanation for the width of the distributions seen (e.g. Fig. 6b).

To explore the nature of the scatter in the single grain D_e data, Fig. 7 plots the overdispersion (OD) as a function of the D_e calculated with the unlogged central age model (CAM; Arnold et al., 2009; Fig. 7) for all 12 samples (Table 3). There is a linear relationship for all but two of the samples (JSH1-2 and JSH1-20, shown in red in Fig. 7); based on this trend these

two samples have higher overdispersion than would be expected for their D_e, and are the samples, which exhibit a clear tail of grains with much higher D_e values (e.g. Fig. 6d). The unimodal nature of the other ten distributions and the linear increase in absolute overdispersion with age means that it is implausible that this overdispersion arises from incomplete bleaching at deposition. This explanation would require that each sample was systematically better-bleached at deposition than those laid-down by earlier events, and there is no reason to expect such a pattern.

The slope of the line in Fig. 7 is 0.45, implying that the relative overdispersion (OD) increases by 45 % of the D_e value. This is higher than the OD value of 20 % typically expected from well-bleached single grains of quartz (Arnold & Roberts, 2009), but there is little feldspar single grain data with which to compare these results. The single grain dose recovery experiments yielded overdispersion values between 10 and 19 %, and so OD values from samples irradiated in nature would be expected to be at least this magnitude. In addition to the sources of overdispersion that affect quartz, single grains of feldspar may have variable rates of anomalous fading, or different K concentrations leading to variable internal doses. Neudorf et al. (2012) observed high overdispersion (~38–47 %) in their single grain feldspar D_e values, a subset of which were corrected for grain-specific fading rates, but could not categorically demonstrate whether this resulted from post-depositional mixing or some other source. Smedley et al. (2016) working on glacial samples from the southern Andes suggested that samples that had overdispersion values of 50 % or less had been well bleached. In light of these results, the slope of 0.45 in Fig. 7 is not unreasonable as the best estimate for the overdispersion characteristic of a well-bleached sample.

Fig. 7 shows that at least two of the samples have much higher OD than would be expected, and hence the minimum age model is applied in order to extract the most appropriate population for age calculation. For consistency, the same age model was used for all samples. Where samples are well bleached the MAM will yield similar results to the CAM.

5.3 Application of the minimum age model

An unlogged 3-parameter minimum age model (MAM; Arnold et al. 2009) was applied to all samples, using overdispersion values derived from the relationship shown in Fig. 7. The unlogged MAM requires that sigma-b (the overdispersion of aliquots or single grains which have been well bleached at deposition) be specified as an absolute dose (in Gy), not as a percentage as required for the logged MAM (Galbraith et al., 1999). Since the absolute overdispersion of these samples seems to depend upon their D_e calculated for the sample (Fig. 7), an iterative approach was used. This involved calculating the OD value for each sample using the relationship shown in Fig. 7 and a D_e value calculated using the unlogged CAM. The OD value was then used as sigma-b to run the MAM model, yielding a new estimate of the D_e for the sample. This new estimate of D_e was then used to determine the OD from the relationship in Fig. 7, and this new value used to rerun the MAM. This iterative process rapidly converged (typically within 2 iterations) to stable values for the D_e and OD (Table 3). For most samples this process resulted in the inclusion of more than 95 % of the D_e values (Table 3), excluding a small number of very high D_e values, and hence confirming that most samples were homogeneously bleached. For the two youngest samples (JSH-MOD3 and –MOD4) a smaller proportion of grains was selected in this process, presumably because any incomplete bleaching at deposition will have a larger impact for younger samples.

The MAM D_e values are broadly similar to the CAM values (Table 3), with the exception of the two samples with much higher OD values (Fig. 7), and the samples from the current beach. In these cases the MAM yields smaller D_e values, as would be expected.

6 Results and discussion

6.1 Comparison with independent age control

Figure 8 shows the fading-corrected $IRSL_{50}$ (pre-IR_{130}) ages determined for the 10 samples collected from two adjacent cores in the Shirasuka lowlands; the equivalent dose (D_e) values underpinning all of these $IRSL_{50}$ (pre-IR_{130}) ages were obtained using a single method of D_e distribution analysis, as outlined above (section 5). All data were corrected for anomalous fading using the average g_{2days}-value (2.48 ± 0.52 %/decade) obtained previously (section 4.2.1). Buylaert et al (2011) have shown that there is no improvement in precision by using aliquot-specific, or sample-specific fading rates. This approach is particularly appropriate in a geological setting where one would expect a similar provenance for all dated samples, as we interpret for the sediments in the cores studied here. The luminescence ages generated cover the age range from the 13th century AD until the mid 20th century AD (Table 4, Fig. 8) and are all in stratigraphic order. Although the central values for the ages of JSH1-6 and -7 (taken 15 cm apart in core JSH1/overlap, from within the same sand unit) are inverted, these samples are in agreement within the 1σ uncertainties shown, indicating rapid deposition and demonstrating the reproducibility of the luminescence analyses within this sand unit (Fig. 8).

The accuracy of the luminescence results can be assessed by comparing the ages with those obtained from radiocarbon dating of wood, and with aerial photography. The first comparison is provided by data from Garrett et al. (accepted) who investigated cores taken adjacent

to those used for luminescence dating in the present study. They obtained calibrated radiocarbon ages on wood from above (AD 1282–1399) and below (AD 1040–1262) the sedimentary unit of sample JSH1-20 in sediment core JSH1b/full. The $IRSL_{50}$ (pre-IR_{130}) age of AD 1390 (± 64 a) for JSH1-20 is consistent with these age estimates (Fig. 8).

A second comparison is for sample JSH1-2 at a depth of 47–53 cm, which is thought to be related to a landslide from the terrace immediately behind the coring site arising from an intense earthquake in AD 1944. The landslide is recorded on aerial photography of the region in AD 1947 (Garrett et al., accepted). The $IRSL_{50}$ (pre-IR_{130}) age of AD 1950 (± 8 a) would support this interpretation. It is interesting to note that this sample has an overdispersion that is higher than would be expected (Fig. 7); this too is consistent with its origin from landsliding. The agreement of the luminescence ages with independent age estimates, and the low residual doses seen in the two beach samples (0.03 ± 0.01 Gy for JSH-MOD3 and 0.12 ± 0.02 Gy for JSH–MOD4, Table 3) implies that when using the $IRSL_{50}$ (pre-IR_{130}) signal from single grains residual signals and thermal transfer are not major impediments (cf. Li et al., 2017).

6.2 Integration with historical records and previous studies

The sedimentary record of the Shirasuka lowlands reveals a complex stratigraphy with laterally discontinuous sand sheets, reflecting deposition by extreme wave events. Radiocarbon dates published by Komatsubara et al. (2008) and Fujiwara et al. (2006) constrain the extreme wave event sedimentary record of the Shirasuka lowlands to be younger than AD 1200. From AD 1200 onwards, at least six earthquakes and subsequent tsunamis occurred in

segment C, D and E (Fig. 1a; Garrett et al., 2016). Additionally, large storm surges were reported to have inundated the lowlands several times (Komatsubara et al., 2008).

Lateral discontinuity between the sand layers recorded in cores taken from this site has previously been described by Komatsubara et al. (2008), and this lateral discontinuity is also noted in this study for cores JSH1b/full and JSH1/overlap even though they are only 0.5 m apart (Fig. 2). However, correlation between the two cores in the present study, and potential links to the record of Komatsubara et al. (2008), can be aided by the luminescence ages generated (Fig. 8). The lowermost sand unit in JSH1b/full (Fig. 2 and Fig. 8) is radiocarbon dated to AD 1040–1262 and is identified as the former beach (Garrett et al., accepted). A minimum age for sand unit 4 in JSH1b/full is given by the radiocarbon age (AD 1282–1399; sampled in sediment core JSH1b/full, see Fig. 8) of plant macrofossils (Garrett et al. accepted), and $IRSL_{50}$ (pre-IR_{130}) ages of AD 1291 ± 78 a (sample JSH1-18, core JSH1/overlap), AD 1364 ± 72 a (sample JSH1-16, core JSH1-/overlap) and AD 1390 ± 64 a (sample JSH1-20; core JSH1-b/full) overlap within 1-2σ uncertainties. Sand 4 (Fig. 2 and Fig. 8) in each core can be correlated on the basis of age with unit A of Komatsubara et al. (2008), which they date to AD 1270–1360 using radiocarbon dating, and which they interpret to be derived from terrace material based upon the mica content. The luminescence ages for sand unit 4 containing JSH1-18, JSH1-16 and -20 (AD 1291 ± 78 a, AD 1364 ± 72 a and AD 1390 ± 64 a) are consistent with the Kōan (also known as Shōhei) earthquake and tsunami, which occurred in AD 1361. Based on the historical documents, this earthquake has so far been interpreted as a rupture of the western segements of the Nankai trough (segment A and B). Ishibashi (2004) mentioned the possibility of a synchronous rupture of the eastern and western segments of the Nankai Trough in 1361, or even the possibility of a separate rupture of the eastern seg-

551 ments two days prior to the earthquake of the segments A and B (Ishibashi and Satake,
552 1998; Ishibashi, 2014). No tsunami deposits in the eastern Nankai region have been reported
553 from this event, but this sand sheet could give the first evidence for tsunami inundation in
554 this region.
555
556 Sand 3 (Figs. 2 and 8) has little chronological control from this study, making correlation be-
557 tween cores on the basis of chronology impracticable. However, sample JSH1-13 from core
558 JSH1/full yields a date of AD 1515 (± 50 a), which correlates well with the Meiō tsunami of
559 AD 1498 (Komatsubara et al.'s unit B). Komatsubara et al. (2008) also correlated their Unit B
560 with the Meiō tsunami on the basis of radiocarbon dating of their core (Fig. 8; AD 1390–
561 1500; Komatsubara et al. 2008), taken ~20 m away from the cores in this study. Inundation
562 of the Enshu-nada coastline by the Meiō tsunami has already been demonstrated (e.g. Fuji-
563 wara et al., 2013), making it a reasonable assumption to find some evidence of this event
564 preserved in the Shirasuka lowlands stratigraphy.
565
566 Continuing upward through the sequences of the two cores, the next dated sand unit (sand
567 2) in each case contains samples JSH1-10 (from core JSH1/full) and JSH1-6 and -7 (from core
568 JSH1/overlap). The three luminescence ages obtained (AD 1610 (± 44 a), AD 1577 (± 64 a)
569 and AD 1614 (± 39 a), respectively) are tightly clustered, and can be correlated with unit C of
570 Komatsubara et al. (2008), which they associated with the AD 1605 Keichō tsunami. The
571 three luminescence ages provide a much more precise association with this event than the
572 radiocarbon ages of Komatsubara et al. (2008) which gave a wide envelope for the age of
573 their Unit C ranging from 1440 to 1640 AD. Sample JSH1-9 comes from the finer deposit that
574 caps this sand unit in core JSH1/full, but was later interpreted to be a rip-up clast. The date

575 of AD 1648 (± 42 a) is also consistent with the underlying sand originating from the AD 1605
576 tsunami. The age of JSH1-9, and the presence of this fine unit between two sand units in
577 core JSH1-full, also implies that the overlying sand units probably relate to a different event.
578 Indeed, the date of AD 1763 (± 23 a) for JSH1-4, taken from the uppermost part of sand unit
579 2, is statistically distinct from the ages obtained for the lowerpart of sand unit 2 (which con-
580 tains JSH-6 and -7), suggesting that unit 2 records two discrete events (labelled 2a and 2b on
581 Fig. 8). It is not immediately obvious what historical event unit 2a correlates with, or which
582 unit of Komatsubara et al. (2008) it might correspond to (i.e. Unit D, E or F), if any. The ex-
583 treme wave event closest in time is the 1707 Hōei tsunami, although the luminescence age is
584 ~2.5 standard deviations from this event. Interestingly, the AD 1751 Concepción (Chile) tsu-
585 nami also lies within the age range from luminescence dating (AD 1763 ± 23 a), and is known
586 to have crossed the Pacific and inundated parts of the Japanese coastline (e.g. Sendai and
587 Wakayama; Atwater et al., 2015); however, there is no historical evidence for inundation
588 along the Enshu-nada coast at this time (Watanabe, 1998).
589
590 As discussed previously, JSH1-2, the uppermost sand unit in core JSH1/full, gave a lumines-
591 cence age of AD 1950 (± 8 a) and this correlates well with the AD 1944 Tōnankai earthquake
592 that affected this region. Although this AD 1944 earthquake caused a tsunami, its wave
593 height (~0.9 m) was too small to overwash the coastal dune. Komatsubara et al. (2008) used
594 radiocarbon dating to constrain their Unit G with which this correlates, describing it as being
595 derived from terrace material, but a radiocarbon plateau at this time meant that the age
596 constraints were very limited (younger than 1800–1930 AD). The luminescence age in the
597 present study (Table 3, Fig. 8) provides a much tighter constraint on the timing of emplace-
598 ment of this sand unit.

7 Summary and conclusions

This study tested the suitability of luminescence dating to constrain the age of young (< 1000 years) extreme wave event deposits from the Shirasuka lowlands, Japan. Unsurprisingly, and in accordance to other studies, quartz was found to be unsuitable for dating. Coarse grains of alkali-feldspar were tested and subsequently used for dating. The $IRSL_{50}$ signal measured as part of a post-IR_{50} $IRSL_{130}$ protocol was found to be most suitable for dating these deposits.

The degree of bleaching of the Shirasuka sediment samples taken for luminescence dating was assessed by examining single coarse-grains of alkali-feldpsars. The $IRSL_{50}$ (pre-IR_{130}) single grain distributions were surprisingly well-bleached, given the expectation that these were taken from extreme wave event deposits. Nevertheless, each sample contained a small proportion of grains with larger-than-expected D_e values, and for each sample the overdispersion values typically scaled with the D_e value. The unlogged minimum age model was therefore applied to the D_e data from these young sediments, using a novel iterative method for estimating the absolute overdispersion value (in Gy). This approach enabled a single method of D_e distribution analysis to be applied to all samples in this study, and resulted in fading-corrected $IRSL_{50}$ (pre-IR_{130}) ages which that were both internally consistent, and that could also be correlated to other evidence for extreme wave events in this region, including the historical record and independent dating evidence.

622 The fading-corrected $IRSL_{50}$ (pre-IR_{130}) ages demonstrate that the two cores in this study
623 span the historical record of extreme wave event deposits in this region. The luminescence
624 ages also demonstrate that it is possible to differentiate between individual events that oc-
625 curred within the past 800 years. These $IRSL_{50}$ (pre-IR_{130}) ages can be linked to the presence
626 and impact of tsunamis in AD 1361, AD 1498, and AD 1605, and also to a slope failure driven
627 by the AD 1944 Tōnankai earthquake. The absence of sand layers driven by other major
628 known extreme wave events in this region, such as the AD 1707 Hōei tsunami and the AD
629 1854 Ansei-Tōnankai earthquake and tsunami events, is potentially due to issues of preser-
630 vation such as lateral discontinuity of the sand sheets.
631
632 In some cases, the luminescence dates generated in this study constrain the extreme wave
633 event units more precisely than the radiocarbon dating, due to plateau within the ^{14}C-
634 calibration curve around the time of interest. This study highlights the great potential for
635 using luminescence dating, including using a signal from feldspars, to date even young ex-
636 treme wave event deposits in both this region, and potentially elsewhere.
637
638
639 **Acknowledgements**
640 This research was undertaken as part of the QuakeRecNankai project, funded by the Belgian
641 Science Policy Office (BELSPO BRAIN-be BR/121/ A2). SR's MSc studies were financially sup-
642 ported by the Deutschlandstipendium scholarship, which is gratefully acknowledged. A re-
643 search stay of SR at the Aberystwyth Luminescence Research Laboratory (ALRL), Aberyst-
644 wyth University (UK) was possible due to a DAAD (German Academic Exchange Service)
645 PROMOS student mobility scholarship. SR would like to thank the Arbeitskreis für Geomor-

phologie (German Working group of Geomorphologists) for financially supporting her participation in the UK Luminescence and ESR meeting 2016, where this work was presented. GEK acknowledges financial support from Swiss National Science Foundation grant PZ00P2_167960. Hollie Wynne (Aberystwyth University, UK) is thanked for her help in the ALRL. Hanna Cieszynski (University of Cologne, Germany) took the REM images. Ian Bailiff (Durham University, UK) is thanked for providing the spreadsheet, which was used to correct for layer-to-layer variations in gamma dose rate according to Aitken (1985). All authors would like to acknowledge the support by local authorities and the landowners, who permitted fieldwork in the paddy fields We would like to thank Dr. Sumiko Tsukamoto and an anonymous referee for their comments, which helped to improve this paper.

This is a contribution to IGCP project 639 “Sea-level changes from minutes to millennia” and INQUA Project CMP1701P.

References

Adamiec, G., Aitken, M.J., 1998. Dose-rate conversion factors: update. Anc. TL 16, 37–50.

Aitken, M.J., 1985. Thermoluminescence Dating. Academic Press, London, 359pp.

Ando, M., 1975. Source mechanisms and tectonic significance of historical earthquakes along the Nankai trough, Japan. Tectonophysics 27, 119–140.

667 Arnold L. J., Roberts R. G., 2009. Stochastic modelling of multi-grain equivalent dose (*De*)
668 distributions: Implications for OSL dating of sediment mixtures. Quat. Geochronology
669 4, 204–230.

670 Arnold, L. J., Roberts, R. G., Galbraith, R. F., DeLong, S. B., 2009. A revised burial dose estima-
671 tion procedure for optical dating of young and modern-age sediments. Quat. Geo-
672 chronol. 4, 306–325.

673 Atwater, B. F., Satoko, M.-R., Kenji, S., Yoshinobu, T., Kazue, U., Yamaguchi, D. K., 2015. The
674 Orphan Tsunami of 1700 – Japanese clues to a parent earthquake in North America.
675 University of Washington Press, Washington, 135 pp.

676 Auclair, M., Lamothe, M., Huot, S., 2003. Measurement of anomalous fading for feldspar
677 IRSL using SAR. Radiat. Meas.37, 487–492.

678 Bell, W.T., 1980. Alpha attenuation in Quartz grains for Thermoluminescence Dating. Anc. TL
679 12, 4–8.

680 Bishop, P., Sanderson, D., Hansom, J., Chaimanee, N., 2005. Age- dating of tsunami deposits:
681 lessons from the 26 December 2004 tsunami in Thailand. Geogr. J. 171, 379–384.

682 Blair, M., Yukihara, E.G., McKeever, S.W.S. 2005. Experiences with single-aliquot OSL proce-
683 dures using coarse-grain feldspars. Radiat. Meas. 39, 361-374.

684 Brill, D., Klasen, N., Jankaew, K., Brückner, H., Kelletat, D., Scheffers, A., Scheffers, S., 2012a.
685 Local inundation distances and regional tsunami recurrence in the Indian Ocean in-
686 ferred from luminescence dating of sandy deposits in Thailand. Nat. Hazards Earth
687 Syst. Sci. 12, 2177–2192.

688 Brill, D., Klasen, N., Brückner, H., Jankaew, K., Scheffers, A., Kelletat, D., Scheffers, S., 2012b.
689 OSL dating of tsunami deposits from Phra Thong Island, Thailand. Quat. Geochronol.
690 10, 224–229.

691 Brill, D., May, M. S., Engel, M., Reyes, M., Pint, A., Opitz, S., Dierick, M., Gonzalo, L. A., Esser,
692 S., Brückner, H., 2016. Typhoon Haiyan's sedimentary record in coastal environments
693 of the Philippines and its palaeotempestological implications. Nat. Hazards Earth Syst.
694 Sci. 16, 7299–2822.

695 Buylaert, J.-P., Huot, S., Murray, A. S., van den Haute, P., 2011. Infrared stimulated lumines-
696 cence dating of an Eemian (MIS 5e) site in Denmark using K-feldspar. Boreas 40, 46–
697 56.

698 Buylaert, J.-P., Murray, A. S., Thomsen, K. J., Thiel, C., Sohbati, R., 2012. A robust feldspar
699 luminescence dating method for Middle and Late Pleistocene sediments. Boreas 41,
700 435–451.

701 Chagué-Goff, C., Schneider, J.-L., Goff, J. R., Dominey-Howes, D., Strotz, L., 2011. Expanding
702 the proxy toolkit to help identify past events – Lessons from the 2004 Indian Ocean
703 Tsunami and the 2009 South Pacific Tsunami. Earth Sci. Rev. 107, 107–122.

704 Colarossi, D., Duller, G.A.T., Roberts, H.M., Tooth, S., Lyons, R., 2015. Comparison of paired
705 quartz OSL and feldspar post-IR IRSL dose distributions in poorly bleached fluvial sed-
706 iments from South Africa. Quat. Geochronol. 30, 233–238.

707 Colarossi, D., Duller, G.A.T., Roberts, H.M. (in press). Exploring the behaviour of lumines-
708 cence signals from feldspars: implications for the single aliquot regenerative dose
709 protocol. Radiat. Meas.

710 Cunha, P. P., Buylaert, J. P., Murray, A. S., Andrade, C., Freitas, M. C., Fatela, F., Munhá, J. M.,
711 Martins, A. A., Sugisaki, S., 2010. Optical dating of clastic deposits generated by an
712 extreme marine coastal flood: The 1755 tsunami deposit in the Algarve (Portugal).
713 Quat. Geochronol. 5, 329–335.

714 Cunningham, A.C., Bakker, M.A.J., van Heteren, S., van der Valk, B., van der Spek, A.J.F.,
715 Schaart, D.R., Wallinga, J., 2011. Extracting storm-surge data from coastal dunes for
716 improved assessment of flood risk. Geology 39 (11), 1063–1066.

717 Dawson, A. G., Stewart, I., 2007. Tsunami deposits in the geological record. Sediment. Geol.
718 200, 166–183.

719 Durcan, J. A., King, G. E., Duller, G. A. T., 2015. DRAC: Dose Rate and Age Calculator for
720 trapped charge dating. Quat. Geochronol. 28, 54–61.

721 Engel, M., Brückner, H., Wennrich, V., Scheffers, A., Kelletat, D., Vött, A., Schäbitz, F., Daut,
722 G., Willershäuser, T., May, S. M., 2010. Coastal stratigraphies of eastern Bonaire
723 (Netherlands Antilles): New insights into the palaeo-tsunami history of the southern
724 Caribbean. Sediment. Geology 231, 14–30.

725 Fujiwara, O., Komatsubara, J., Takada, K., Shishikura, M., Kamataki, T., 2006. Temporal de-
726 velopment of a late Holocene strand plain system in the Shirasuka area along west-
727 ern Shizuoka Prefecture on the Pacific coast of central Japan. Chigaku Zasshi 115,
728 569–581 (In Japanese).

729 Fujiwara, O., Ono, E., Yata, T., Umitsu, M., Sato, Y., Heyvaert, V. M. A., 2013. Assesing the
730 impact of 1498 Meio earthquake and tsunami along the Enschu-nada coast, central
731 Japan using coastal geology. Quat. Int. 308–309, 4–12.

732 Galbraith, R. F., Roberts, R. G., Laslett, G. M., Yoshida, H., Olley, J. M., 1999. Optical dating of

single and multiple grains of quartz from Jinmium Rock Shelter, Northen Australia: Part I, experimental design and statistical models. Archaeometry 41 (2), 339–364.

Garrett, E., Fujiwara, O., Garrett, P., Heyvaert, V. M. A., Shishikura, M., Yokoyama, Y., Hubert-Ferrari, A., Brückner, H., Nakamura, A., De Batist, M., the QuakeRecNankai team, 2016. A systematic review of geological evidence for Holocene earthquakes and tsunamis along the Nankai-Suruga Trough, Japan. Earth Sci. Rev. 159, 337–357.

Garrett E., Fujiwara, O., Riedesel, S., Walstra, J., Deforce, K., Yokoyama, Y., Schmidt, S., Brückner, H., De Batist, M., Heyvaert, V.M.A., QuakeRecNankai team, accepted. Historical Nankai-Suruga megathrust earthquakes recorded by tsunami and terrestrial mass movement deposits on the Shirasuka coastal Lowlands, Shizuoka Prefecture, Japan. The Holocene. DOI: 10.1177/0959683617752844

Goff, J., Ebina, Y, Goto, K., Terry, J., 2016. Defining tsunamis: Yoda strikes back? Earth Sci. Rev. 159, 271–274.

Guérin, G., Mercier, N., Nathan, R., Adamiec, G., Lefrais, Y., 2012. On the use of the infinite matrix assumption and associated concepts: A critical review. Radiat. Meas., 47, 778–785.

Huntley, D. J., Clague, J. J., 1996. Optical dating of tsunami-laid sands. Quat. Res. 46, 127–140.

Huntley, D. J., Lamothe, M., 2001. Ubiquity of anomalous fading in K-feldspars and the measurement and correction for it in optical dating. Can. J. Earth Sci. 38, 1093–1106.

Ishibashi, K. 2014. Nankai Trough great earthquake – History, Science and Society. Tokyo, Iwanami Shoten, 205pp.

Ishibashi, K., Satake, K., 1998. Problems on forecasting great earthquakes in the subduction zones around Japan by means of paleoseismology. Zisin 50, 1–21.

Ishibashi, K., 2004. Status of historical seismology in Japan. Ann. Geophys. 47 (2/3), 339–368.

Jankaew, K., Atwater, B. F., Sawai, Y., Choowong, M., Charoentitirat, T., Martin, M. E., Prendergast, A., 2008. Medieval forewarning of the 2004 Indian Ocean tsunami in Thailand. Nature 455, 1228–1231.

Kars, R.H., Reimann, T., Ankjaergaard, C., Wallinga, J. 2014. Bleaching of the post-IR IRSL signal: new insights for feldspar luminescence dating. Boreas 43, 780-791.

Komatsubara, J., Fujiwara, O., Takada, K., Sawai, Y., Aung, T. T., Kamataki, K., 2008. Historical tsunamis and storms recorded in a coastal lowland, Shizuoka Prefecture, along the Pacific Coast of Japan. Sedimentology 55, 1703–1716.

Kondo, R., Tsukamoto, S., Tachibana, H., Miyairi, Y., Yokoyama, Y., 2007. Age of glacial and periglacial landforms in northern Hokkaido, Japan, using OSL dating of fine grain quartz. Quat. Geochronol. 2, 260–265.

Kreutzer, S., Schmidt, C., Fuchs, M. C., Dietze, M., Fischer, M., Fuchs, M., 2012. Introducing an R package for luminescence dating analysis. *Ancient TL* 30(1): 1–8.

Kreutzer, S. (2016). calc_FadingCorr(): Apply a fading correction according to Huntley & Lamothe (2001) for a given g-value and a given tc. Function version 0.4.2. In: Kreutzer, S., Dietze, M., Burow, C., Fuchs, M.C., Schmidt, C., Fischer, M., Friedrich, J. (2016). Luminescence: Comprehensive Luminescence Dating Data Analysis. R package version 0.6.4. https://CRAN.R-project.org/package=Luminescence

776 Li, Y., Tsukamoto, S., Hu, K., Frechen, M., 2017. Quartz OSL and K-feldspar post-IR IRSL dating
777 of sand accumulation in the lower Liao Plain (Liaoning, NE China). Geochronometria
778 44, 1-15.

779 Loveless, J.P., Meade, B.J., 2010. Geodetic imaging of plate motions, slip rates, and
780 partitioning of deformation in Japan. J. Geophys. Res. 115, B02410.

781 Madsen, A., T., Buylaert, J-P., Murray, A. S., 2011. Luminescence dating of young coastal de-
782 posits from New Zealand using feldspars. Geochronometria 38 (4), 378–390.

783 Madsen, A.T., Duller, G.A.T., Donnelly, J.P., Roberts, H.M., Wintle, A.G., 2009. A chronology
784 of hurricane landfalls at Little Sippewissett Marsh, Massachusetts, USA, using optical
785 dating. Geomorphology 109, 36–45.

786 Madsen, A. T., Murray, A. S., 2009. Optically stimulated luminescence dating of young sedi-
787 ments: A review. Geomorphology 109, 3–16.

788 May, S. M., Falvard, S., Norpoth, M., Pint, A., Brill, D., Engel, M., Scheffers, A., Dierick, M.,
789 Paris, R., Squire, P., Brückner, H., 2016. A mid-Holocene candidate tsunami deposit
790 from the NW Cape (Western Australia). Sediment. Geol. 332, 40–50.

791 Mazzotti, S., Le Pichon, X., Henry, P., Miyazaki, S., 2000. Full interseismic locking of the Nan-
792 kai and Japan-west Kurile subduction zones: an analysis of uniform elastic strain ac-
793 cumulation in Japan constrained by permanent GPS. J. Geophys. Res. Solid Earth 105,
794 13159–13177.

795 Monecke, K., Finger, W., Klarer, D., Kongko, W., McAdoo, B. G., Moore, A. L., Sudrajat, S. U.,
796 2008. A 1,000-year sediment record of tsunami recurrence in northern Sumatra. Na-
797 ture 455 (30), 1232–1234.

798 Morton, R. A., Gelfenbaum, G., Jaffe, B. E., 2007. Physical criteria for distinguishing sandy
799 tsunami and storm deposits using modern examples. Sediment. Geol. 200, 184–207.

800 Murari, M. K., Achyuthan, H., Singhvi, A. K., 2007. Luminescence studies on the sediments
801 laid down by the December 2004 tsunami event: Prospects for the dating of palaeo
802 tsunamis and for the estimation of sediment fluxes. Science 92 (3), 367–371.

803 Murray, A.S., Wintle, A.G., 2003. The single aliquot regenerative dose protocol: potential for
804 improvements in reliability. Radiat. Meas. 37, 377–381.

805 Murray, A.S., Buylaert, J.P., Thomsen, K.J., Jain, M., 2009. The effect of preheating on the
806 IRSL signal from feldspar. Radiat. Meas. 44, 554–559.

807 Neudorf, C.M., Lian, O.B., Walker, I.J., Shugar, D.H., Eamer, J.B.R., Griffin, L.C.M., 2015. To-
808 ward a luminescence chronology for coastal dune and beach deposits on Calvert Is-
809 land, British Columbia central coast, Canada. Quat. Geochron. 30, 275–281.

810 Neudorf, C.M., Roberts, R.G., Jacobs, Z., 2012. Sources of overdispersion in a K-rich feldspar
811 sample from north-central India: Insights from D_e, K content and IRSL age distribu-
812 tions for individual grains. Radiat. Meas. 47, 696–702.

813 Pilarczyk, J. E., Horton, B. P., Soria, J. L. A., Switzer, A. D., Siringan, F., Fritz, H. M., Khan, N. S.,
814 Ildefonso, S., Doctor, A. A., Garcia, M. I., 2016. Micropaleontology of the 2013 Ty-
815 phoon Haiyan overwash sediments from the Leyte Gulf, Philippines. Sediment. Geol.
816 339, 104–114.

817 Prendergast, A. L., Cupper, M. L., Jankaew, K., Sawai, Y., 2012. Indian Ocean tsunami recur-
818 rence from optical dating of tsunami sand sheets in Thailand. Mar. Geol. 295–298,
819 20–27.

820 Prescott, J.R., Hutton, J.T., 1994. Cosmic ray contributions to dose rates for lumi-
821 nescence and ESR dating: large depths and long-term time variations. Radiat.
822 Meas. 23, 497–500.
823 Reimann, T., Tsukamoto, S., 2012. Dating the recent past (<500) by post-IR IRSL feldspar –
824 Examples from the North Sea and Baltic Sea coast. Quat. Geochronol. 10, 180–187.
825 Reimann, T., Thomsen, K.J., Jain, M., Murray, A.S., Frechen, M., 2012. Single-grain dating of
826 young sediments using the pIRIR signal from feldspar. Quat. Geochronol. 11, 28–41.
827 Satake, K., 2015. Geological and historical evidence of irregular recurrent earthquakes in
828 Japan. Phil. Trans. R. Soc. A 373, 1–10.
829 Shanmugam, G., 2012. Process-sedimentological challenges in distinguishing paleo-tsunami
830 deposits. Nat. Hazards 63, 5–30.
831 Smedley, R.K., Glasser, N.F., Duller, G.A.T., 2016. Luminescence dating of glacial advances at
832 Lago Buenos Aires (~46 °S), Patagonia. Quat. Sci. Rev. 134, 59–73.
833 Smedley, R.K., Duller, G. A. T., Pearce, N. J. G., Roberts, H. M., 2012. Determining the K-
834 content of single-grains of feldspar for luminescence dating. Radiat. Meas. 47, 790–
835 796.
836 Soria, J. L. A., Switzer, A. D., Pilarczyk, J. E., Siringan, F. P., Khan, N. S., Fritz, H. M., 2017. Ty-
837 phoon Haiyan overwash sediments from Leyte Gulf coastlines show local spatial vari-
838 ations with hybrid storm and tsunami signatures. Sediment. Geol. 358, 121–138.
839 Spiske, M., Piepenbreier, J., Benavente, C., Kunz, A., Bahlburg, H., Steffahn, J., 2013. Histori-
840 cal tsunami deposits in Peru: Sedimentology, inverse modelling and optically stimu-
841 lated luminescence dating. Quat. Int. 305, 31–44.

842 Steffen, D., Preusser, F., Schlunegger, F., 2009. OSL quartz age underestimation due to un-
843 stable signal components. Quat. Geochronol. 4, 353–362.

844 Stuiver, M., 1978. Radiocarbon timescale tested against magnetic and other dating methods.
845 Nature 273, 271–274.

846 Switzer, A. D., Srinivasalu, S., Thangadurai, N., Ram Mohan, V., 2012. Bedding structures in
847 Indian tsunami deposits provide clues to the dynamics of tsunami inundation. In: Ter-
848 ry, J., Goff, J. (eds.), 2012. Natural Hazards in the Asia – Pacific Region: Recent Ad-
849 vantages and Emerging Concepts. Geol. Soc. London Spec. Pub., London, 361, 61–77.

850 Tamura, T., Sawai, Y., Ito, K., 2015. OSL dating of the AD 869 Jogan tsunami deposit, north-
851 eastern Japan. Quat. Geochronol. 30, 294–298.

852 Thiel, C., Buylaert, J.-P., Murray, A., Terhorst, B., Hofer, I., Tsukamoto, S., Frechen, M., 2011.
853 Luminescence dating of the Stratzing loess profile (Austria) – Testing the potential of
854 an elevated temperature post-IR IRSL protocol. Quat. Intern. 234, 23–31.

855 Thomsen, K. J., Murray, A. S., Jain, M., Bøtter-Jensen, L., 2008. Laboratory fading rates of
856 various luminescence signals from feldspar-rich sediment extracts. Radiat. Meas. 43,
857 1474–1486.

858 Tsukamoto, S., Rink, W. J., Watanuki, T., 2003. OSL of tephric loess and volcanic quartz in
859 Japan and an alternative procedure for estimating De from a fast OSL component.
860 Radiat. Meas. 37, 459–465.

861 Usami, T., 1979. Study of Historical Earthquakes in Japan. Bulletin of the Earthquake Re-
862 search Institute 54, 399–439.

863 Wallinga, J., Murray, A.S., Wintle, A.G., 2000. The single-aliquot regenerative-dose (SAR) pro-
864 tocol applied to coarse-grain feldspar. Radiat. Meas. 32, 529–533.
865 Watanabe, H., 1998. Comprehensive list of tsunamis to hit the Japanese islands [second edi-
866 tion]. University of Tokyo Press, Tokyo, 238pp.
867 Wintle, A.G., 1973. Anomalous fading of thermoluminescence in mineral samples. Nature
868 245, 143–144.
869

870 Tables

Sample[a]	Lab Code	Core	Depth (cm)	U (ppm)	Th (ppm)	K %	Water content (%)[b]	Internal K[c]	Multi-layer gamma dose rate (Gy/ka)	Cosmic dose rate (Gy/ka)	Environmental dose rate (Gy/ka)[d]
JSH1-2	**C-L3944**	**JSH1b-full**	47 - 53	2.30 ± 0.40	18.2 ± 1.2	1.72 ± 0.13	13.9	8.23 ± 0.44	1.28 ± 0.15	0.20 ± 0.02	3.83 ± 0.31
JSH1-4	**C-L3946**	**JSH1 OL**	77 - 82	2.25 ± 0.14	25.4 ± 1.5	1.57 ± 0.02	28.2	7.78 ± 052	1.57 ± 0.13	0.19 ± 0.02	3.92 ± 0.26
JSH1-6	**C-L3948**	**JSH1 OL**	112 - 117	2.70 ± 0.40[e]	32.6 ± 2.0[e]	1.57 ± 0.13[e]	22.6	n.d.	1.41 ± 0.18	0.18 ± 0.02	4.06 ± 0.33
JSH1-7	**C-L3949**	**JSH1 OL**	125 - 134				30.0	6.24 ± 0.58	1.39 ± 0.16	0.17 ± 0.02	3.91 ± 0.3
JSH1-9	**C-L3951**	**JSH1b-full**	133 - 137	2.14 ± 0.13	31.2 ± 1.8	1.47 ± 0.02	34.6	6.84 ± 0.26	1.52 ± 0.14	0.17 ± 0.02	3.82 ± 0.26
JSH1-10	**C-L3952**	**JSH1b-full**	144 - 146	2.80 ± 0.50	31.3 ± 2.1	1.54 ± 0.12	19.5	4.44 ± 0.59	1.38 ± 0.19	0.17 ± 0.02	4.06 ± 0.34
JSH1-13	**C-L3955**	**JSH1b-full**	185 - 194	2.11 ± 0.12	32.5 ± 1.9	1.42 ± 0.02	19.1	5.82 ± 0.43	1.10 ± 0.18	0.16 ± 0.02	3.65 ± 0.31
JSH1-16	**C-L3958**	**JSH1 OL**	215 - 219	1.20 ± 0.30	17.0 ± 1.1	1.34 ± 0.18	24.9	6.55 ± 0.57	0.86 ± 0.11	0.16 ± 0.02	2.80 ± 0.26
JSH1-18	**C-L3960**	**JSH1 OL**	235 - 244	1.54 ± 0.29	19.7 ± 1.3	1.47 ± 0.11	18.9	5.96 ± 0.34	0.75 ± 0.13	0.15 ± 0.02	2.95 ± 0.27
JSH1-20	**C-L3962**	**JSH1b-full**	269 - 279	2.20 ± 0.40	20.7 ± 1.3	1.57 ± 0.12	19.1	6.09 ± 0.51	1.01 ± 0.14	0.15 ± 0.02	3.37 ± 0.29

871
872 Notes:
873 a) Grain size for all samples was 100-200 µm.
874 b) Measured water content values used in the calculation of dose rate, to which an uncertainty of ± 10% was applied.
875 c) Internal K content was measured for each sample, but for dose rate calculations a value of 10 ± 2 % was assumed, resulting in an internal beta dose of 0.502 ± 0.167
876 Gy/ka for all samples.
877 d) Alpha efficiency value of 0.072 ± 0.003 used (see Supplementary Information for methods used to determine alpha-efficiency).
878 e) A single dosimetry sample was measured for JSH1-6 and JSH1-7 due to their close proximity.
879
880
881 Table 1: U, Th and K concentrations derived from high resolution gamma spectrometry, measured water content, internal K content derived from
882 beta counting, and values of the cosmic dose rate derived from the burial depth and geographical position of the coring location. The gamma dose
883 rate given here was calculated using all layers influencing the luminescence samples, according to Aitken (1985).

884

885 (a) $IRSL_{50}$ - MG

Step	Treatment	Observed
1	Regenerative dose	
2	Preheat at 190°C for 10 s	
3	IRSL Measurement (diodes) at 50 °C for 200 s	L_x
4	Test dose	
5	Preheat at 190°C for 10 s	
6	IRSL Measurement (diodes) at 50 °C for 200 s	T_x

886

887 (b) Post-IR IRSL - MG

Step	Treatment	Observed
1	Regenerative dose	
2	Preheat at 160°C for 10 s	
3	IRSL Measurement (diodes) at 50 °C for 200 s	L_{x1}
4	IRSL Measurement (diodes) at 130 °C for 200 s	L_{x2}
5	Test dose	
6	Preheat at 160°C for 10 s	
7	IRSL Measurement (diodes) at 50 °C for 200 s	T_{x1}
8	IRSL Measurement (diodes) at 130 °C for 200 s	T_{x2}

888

889 (c) Post-IR IRSL - SG

Step	Treatment	Observed
1	Regenerative dose	
2	Preheat at 160°C for 10 s	
3	IRSL Measurement (laser) at 50 °C for 2 s	L_{x1}
4	IRSL Measurement (laser) at 130 °C for 2 s	L_{x2}
5	Test dose	
6	Preheat at 160°C for 10 s	
7	IRSL Measurement (laser) at 50 °C for 2 s	T_{x1}
8	IRSL Measurement (laser) at 130 °C for 2 s	T_{x2}

890 Table 2: Measurement protocols used. MG = multiple grains, SG = single grains.

891

Sample	n	CAM D_e (Gy)	CAM OD (Gy)	Calc. OD (Gy)[a]	Iterated OD (Gy)[b]	MAM D_e (Gy)	Proportion of D_e values included[c]
JSH-MOD3	249	0.11 ± 0.01	0.17	0.13	0.09	0.03 ± 0.01	0.64
JSH-MOD4	198	0.18 ± 0.02	0.23	0.16	0.13	0.12 ± 0.02	0.89
JSH1-2	240	1.14 ± 0.25	3.81	0.59	0.17	0.21 ± 0.02	0.84
JSH1-4	171	0.90 ± 0.04	0.52	0.48	0.45	0.82 ± 0.04	0.96
JSH1-6	110	1.47 ± 0.06	0.63	0.74	0.74	1.47 ± 0.18	1.00
JSH1-7	107	1.34 ± 0.07	0.65	0.68	0.67	1.30 ± 0.07	0.98
JSH1-9	90	1.16 ± 0.05	0.41	0.60	0.60	1.17 ± 0.10	1.00
JSH1-10	85	1.52 ± 0.10	0.88	0.77	0.68	1.37 ± 0.09	0.95
JSH1-13	114	1.59 ± 0.08	0.75	0.80	0.75	1.51 ± 0.08	0.97
JSH1-16	130	1.57 ± 0.07	0.70	0.79	0.76	1.50 ± 0.07	0.98
JSH1-18	111	2.01 ± 0.12	1.20	0.99	0.87	1.76 ± 0.09	0.94
JSH1-20	104	2.19 ± 0.27	2.70	1.07	0.86	1.74 ± 0.09	0.96

Notes:
a) The calculated OD is the value derived for each sample from the relationship shown in Fig. 7.
b) The iterated OD is the final value of OD obtained after applying the procedure described in section 5.3
c) The p0 parameter obtained from the minimum age model

Table 3: Single grain equivalent dose data for the two samples from the modern beach and the 10 samples from the two cores. D_e values were obtained using the $IRSL_{50}$ (pre-IR_{130}) signal of the post-IR IRSL protocol (Table 2c). The number of D_e values (n) that passed acceptance criteria is shown, along with the unlogged CAM D_e, and the overdispersion calculated for the entire D_e data set for each sample.

Sample	Fading ($g_2$days, %/decade)	MAM D_e (Gy)	Dose Rate (Gy/ka)	Fading corrected age (a)[a]	Date (AD)[b]
JSH1-2	2.72 ± 1.24	0.21 ± 0.02	3.83 ± 0.31	65 ± 8	1950 ± 8
JSH1-4	2.52 ± 1.24	0.82 ± 0.04	3.92 ± 0.27	252 ± 23	1763 ± 23
JSH1-6	3.09 ± 1.31	1.47 ± 0.18	4.06 ± 0.33	438 ± 64	1577 ± 64
JSH1-7	2.07 ± 1.27	1.30 ± 0.07	3.91 ± 0.30	401 ± 39	1614 ± 39
JSH1-9	2.84 ± 1.25	1.17 ± 0.10	3.82 ± 0.26	367 ± 42	1648 ± 42
JSH1-10	3.17 ± 1.26	1.37 ± 0.09	4.06 ± 0.34	405 ± 44	1610 ± 44
JSH1-13	1.84 ± 1.23	1.51 ± 0.08	3.65 ± 0.31	500 ± 50	1515 ± 50
JSH1-16	1.91 ± 1.24	1.50 ± 0.07	2.80 ± 0.26	651 ± 72	1364 ± 72
JSH1-18	1.86 ± 1.23	1.76 ± 0.09	2.95 ± 0.27	724 ± 78	1291 ± 78
JSH1-20	2.76 ± 1.25	1.74 ± 0.09	3.37 ± 0.29	625 ± 64	1390 ± 64

Notes:
a) Ages have been fading corrected using the average fading rate of 2.48 ±0.52 %/decade.
b) Dates have been calculated using a datum of AD 2015 when the samples were collected.

Table 4: Fading rates, D_e values, dose rates and ages for the 10 samples from the cores. D_e values were obtained using the $IRSL_{50}$ (pre-IR_{130}) signal of the post-IR IRSL protocol (Table 2c).

Figure Captions:

Fig. 1. Geographical and tectonic setting of the Shirasuka lowlands. (a) Geographical location of the broader study area, tectonic situation and geographical position of the Shirasuka lowlands (source: GeoMapApp (http://www.geomapapp.org); (b) sampling locations of modern beach sediments (JSH-MOD3 from the wet beach, and JSH–MOD4 from the dry beach) and the various sediment cores discussed in the text (source: Google Earth, Terra Metrics, image taken on 27th February 2017).

Fig. 2. Sediment cores JSH1b/full and JSH1/overlap taken for this study. Four sand layers (labelled 1 to 4) are observed, and units 2, 3 and 4 can be correlated between the two cores. Location of dosimetry, OSL and radiocarbon samples (from Garrett et al., accepted) in the cores are given.

Fig. 3. Preheat plateau test results (values are arithmetic mean and standard deviation of three aliquots per temperature), signals and dose response curves for the $IRSL_{50}$ protocol (Table 2a).

Fig. 4. Preheat plateau test results (values are arithmetic mean and standard deviation of three aliquots per temperature), including dose recovery ratios (DRR), residuals, signals and dose-response curves of feldspars. (a-e) for the $IRSL_{50}$ (pre-IR_{elev}) signal within a pIR-IRSL protocol; (f-j) for the post-IR $IRSL_{elev}$ signal within the same protocol. Decay curves and dose-

939 response curves are shown for the highlighted preheat temperatures, which were also used
940 for D_e determination.

941

942 Fig. 5. Changes in response to the test dose during a SAR sequence for the $IRSL_{50}$ (Table 2a),
943 $IRSL_{50}$ (pre-IR_{130}) and the post-IR $IRSL_{130}$ signals (Table 2b and c, respectively). The regenera-
944 tive doses given in cycles 1 to 6 were 0.6, 1.2, 1.8, 2.6, 0.0 and 1.2 Gy respectively.

945

946 Fig. 6. Single grain dose distribution, shown as a Kernel Density Estimate (KDE) plot for (a)
947 JSH-MOD3, (b) JSH1-9, (c) JSH1-6 and (d) JSH1-2. Note the different x-axis scale in (d).

948

949 Fig. 7. Relationship between equivalent dose and the overdispersion (both calculated using
950 the unlogged CAM) of the 12 single grain D_e data sets. The fitted line has a slope of 0.45 and
951 an intercept of 0.08 Gy

952

953 Fig. 8. Stratigraphy and chronology based on $IRSL_{50}$ (pre-IR_{130}) ages for the Shirasuka low-
954 lands, in comparison to previous results by Komatsubara et al. (2008). Sand layers 1, 2, 3 and
955 4 identified in Fig. 2 are shown. Based on the IRSL ages, unit 2 is thought to represent two
956 closely spaced events (2a and 2b). Letters A to G are sands related to events idenitified by
957 Komatsubara et al. (2008). The presented radiocarbon ages are published in Garrett et al.
958 (accepted).

959

960

Supplementary Material

Quartz OSL measurements

Instrumentation for quartz luminescence measurements

Quartz luminescence measurements were performed on a Risø TL/OSL DA 20 reader equipped with a $^{90}Sr/^{90}Y$ beta source delivering ~0.0837 Gy/s at the sample position, blue LEDs (470Δ20 nm) and a Hoya U340 filter (7.5 mm) at the Cologne Luminescence Lab (CLL). The measurement procedure followed the single-aliquot regenerative dose (SAR) protocol (Murray & Wintle, 2003). Aliquots were preheated to 180 °C for 10 s and stimulated at 125 °C for 40 s for Lx determination. Tx was determined by heating to a temperature of 160 °C with immediate cooling, and stimulating for 40 s at 125 °C. The SAR procedure included seven regenerative cycles, including zero dose measurement, regenerative cycle, and a test for IR sensitivity (IR LED stimulation for 40 s at 50°C; Duller, 2003).

Mineralogical investigations

X-ray diffraction was performed for etched quartz grains of selected samples to check for feldspar contamination. For this, etched quartz grains were ground to a homogenous powder and mounted on PVC slides. A Powder X-Ray Diffractometer (Siemens D 5000) with a fixed focal distance of 0.5 mm was used for the mineralogical analysis. The sample was measured at 5–75° 2Θ in 0.05° steps, 10 s/degree. The Cu-K- α source operated at 40 keV and 40 mA. The data were analysed using the DiffracPlus EVA software package (Bruker AXS, Berlin, Germany). Raster electron microscopy (REM) was performed at the Institute of Geology, University of Cologne, with a CamScan 44 Editior and an EDX-microprobe.

Evaluating quartz luminescence measurements

The OSL decay curves of all measured quartz samples reveal relatively low signal intensities for both the natural and regenerative dose signals (Fig. S1). Continuous wave optically stimulated luminescence (CW-OSL) curve fitting demonstrates the absence of a fast component. Instead, high signal intensities as a response to IR stimulation indicate feldspar contamination. However, none of the quartz grains produced any signal significantly different from the background level when exposed to green laser (532 nm) stimulation, and XRD as well as REM measurements indicate pure quartz extracts (Fig. S1). Therefore, we infer that feldspar contamination does not affect the samples. Other studies of quartz from Japan (e.g. Tsukamoto et al., 2003; Tamura et al., 2015) have also observed that the signal is often weak and inappropriate for dating.

Alpha efficiency

For the determination of the alpha-efficiency the heating procedure of Kreutzer et al (2014) was used. Therefore, fine grain (4–11 µm) aliquots were heated to 450 °C by conducting a TL measurement on a Risø TL/OSL DA 20 reader, and subsequently alpha irradiated (calibrated source delivering ~0.197 Gy/s) in a Lexsyg Research instrument. Afterwards, the equivalent dose was measured on a Risø TL/OSL DA 20 reader with a $^{90}Sr/^{90}Y$ beta source delivering ~0.076 Gy/s**.**

Alpha efficiency was determined as 0.072 ± 0.003 for the $IRSL_{50}$ (pre-IR_{130}) signal and as 0.095 ± 0.008 for the post-IR $IRSL_{130}$ signal, based on measurements of two samples (JSH1-4 and JSH1-10). The values are in good agreement with the values presented by Kreutzer et al. (2014), who also observed a difference between the a-value for $IRSL_{50}$ and post-IR IRSL sig-

1010 nals. The a-values after heating presented by Kreutzer et al. (2014) range from 0.072 ± 0.001
1011 to 0.079 ± 0.001 for the $IRSL_{50}$ and from 0.104 ± 0.002 to 0.118 ± 0.002 for the post-IR
1012 $IRSL_{225}$. The difference between the a-value for the post-IR $IRSL_{130}$ signal (this study) and the
1013 a-value for the post-IR$IRSL_{225}$ signal (Kreutzer et al., 2014) might be caused by the tempera-
1014 ture difference of the preheat and the post-IR IRSL stimulation.
1015
1016 **References**
1017 Duller, G. A. T., 2003. Distinguishing quartz and feldspar in single grain luminescence meas-
1018 urements. Radiat. Meas. 37, 161–165.
1019 Kreutzer, S., Schmidt, C., DeWitt, R., Fuchs, M., 2014. The a-value of polymineral fine grain
1020 samples measured with the post-IR IRSL protocol. Radiat. Meas. 69, 18–29.
1021 Tamura, T., Sawai, Y., Ito, K., 2015. OSL dating of the AD 869 Jogan tsunami deposit, north-
1022 eastern Japan. Quat. Geochronol. 30, 294 298.
1023 Tsukamoto, S., Rink, W. J., Watanuki, T., 2003. OSL of tephric loess and volcanic quartz in
1024 Japan and an alternative procedure for estimating De from a fast OSL component.
1025 Radiat. Meas. 37, 459–465.

Dosimetry Sample ID	Sediment core	Depth below surface (cm)	Related OSL sample	U (ppm)	Th (ppm)	K (%)	Water content (meas. %)
1Dn	JSH1b-full	41 ± 2	JSH1-2	2.05 ± 0.12	22.05 ± 1.28	1.54 ± 0.02	19.50
2Dn	JSH1b-full	50 ± 3	JSH1-2	2.30 ± 0.40	18.20 ± 1.20	1.72 ± 0.13	13.90
3Dn	JSH1b-full	58 ± 2	JSH1-2, JSH1-4	2.29 ± 0.12	25.87 ± 1.50	1.69 ± 0.02	28.80
4Dn	JSH1-OL	81 ± 4	JSH1-4	2.25 ± 0.14	25.38 ± 1.48	1.57 ± 0.02	28.20
5Dn	JSH1-OL	90 ± 3	JSH1-6	2.17 ± 0.12	30.59 ± 1.76	1.55 ± 0.02	19.90
6Dn7Dn	JSH1-OL	115 ± 3	JSH1-6, JSH1-7	2.70 ± 0.40	32.60 ± 2.00	1.57 ± 0.13	26.00
8Dn	JSH1-OL	145 ± 2	JSH1-7	2.25 ± 0.14	27.07 ± 1.57	1.54 ± 0.02	74.50
9Dn	JSH1b-full	135 ± 2	JSH1-9, JSH1-10	2.14 ± 0.13	31.22 ± 1.8	1.47 ± 0.02	34.60
10Dn	JSH1b-full	145 ± 2	JSH1-9, JSH1-10	2.80 ± 0.50	31.30 ± 2.10	1.54 ± 0.12	19.50
11Dn12Dn	JSH1b-full	178 ± 2	JSH1-9, JSH1-10, JSH1-13	2.25 ± 0.14	25.38 ± 1.48	1.57 ± 0.02	61.80
13Dn	JSH1b-full	190 ± 5	JSH1-13	2.11 ± 0.12	32.54 ± 1.87	1.42 ± 0.02	19.10
14Dn15Dn	JSH1-OL	192 ± 2	JSH1-13, JSH1-16	2.28 ± 0.14	25.78 ± 1.50	1.57 ± 0.02	71.50
16Dn	JSH1-OL	217 ± 2	JSH1-16	1.20 ± 0.30	17.00 ± 1.10	1.34 ± 0.18	24.90
17Dn	JSH1-OL	230 ± 2	JSH1-16, JSH1-18	1.80 ± 0.40	19.70 ± 1.30	1.47 ± 0.11	105.00
18Dn	JSH1-OL	240 ± 5	JSH1-18	1.54 ± 0.29	19.70 ± 1.30	1.47 ± 0.11	18.90
19Dn	JSH1b-full	260 ± 2	JSH1-20	2.30 ± 0.40	16.30 ± 1.10	1.38 ± 0.12	127.20
20Dn	JSH1b-full	272 ± 5	JSh1-20	2.20 ± 0.40	20.70 ± 1.30	1.57 ± 0.12	19.10
21Dn	JSH1b-full	145 ± 2	JSH1-18, JSH1-20	2.24 ± 0.13	19.48 1.140	1.71 ± 0.02	59.30

Table S1: Results of gamma spectrometry and water content determination.

Figure caption:

Fig. S1: Response of quartz to different stimulation wavelength and mineralogical investigations. a) X-ray diffractogram of etched quartz grains, b) response of etched coarse grain quartz to blue and IR stimulation using diodes, c) REM image of an etched quartz grain, d) response of a single grain of quartz to green laser stimulation, e) response of etched quartz on a single grain disc to IR diode stimulation.

1033 Fig. 1

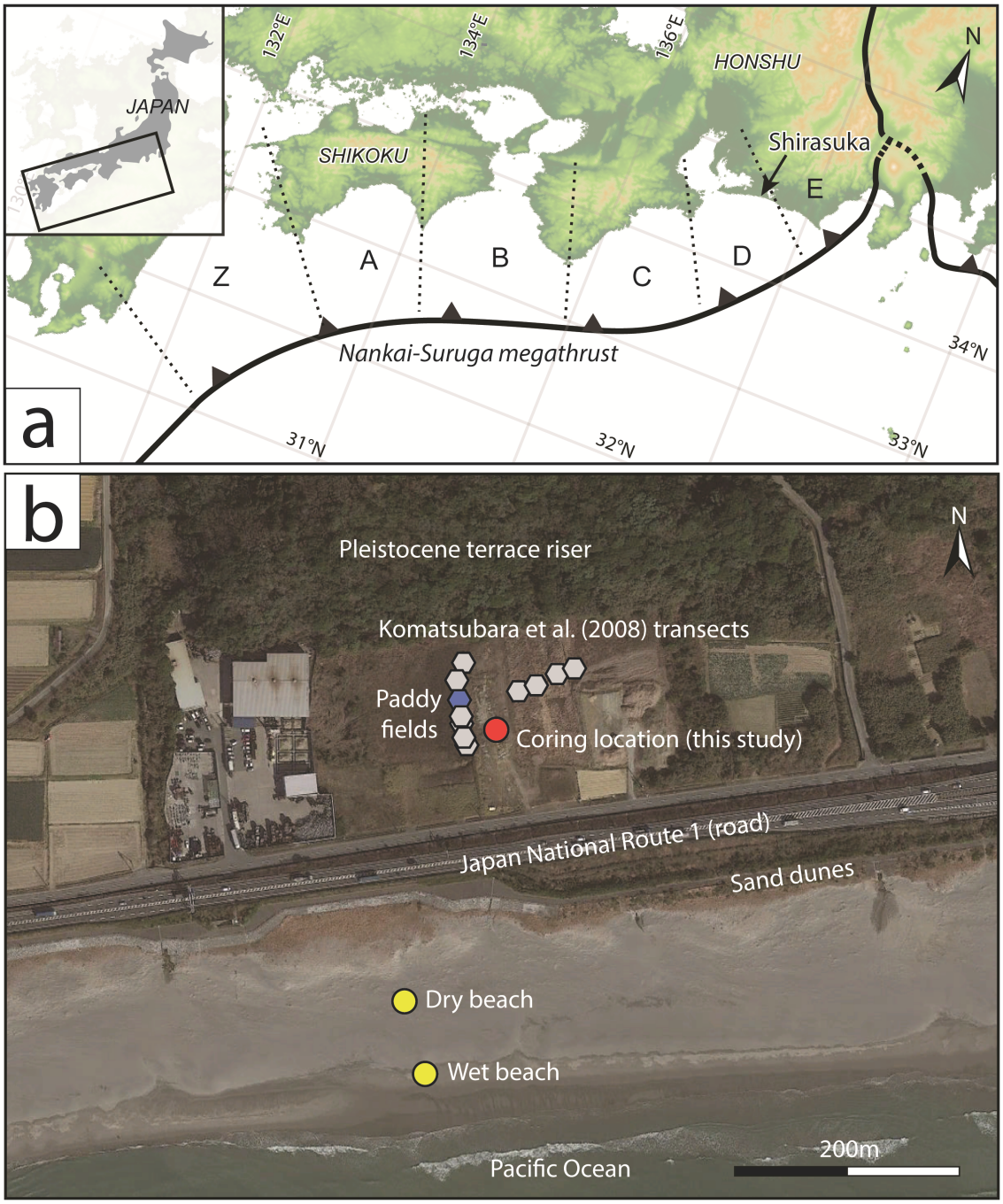

1034
1035
1036

1037 Fig. 2

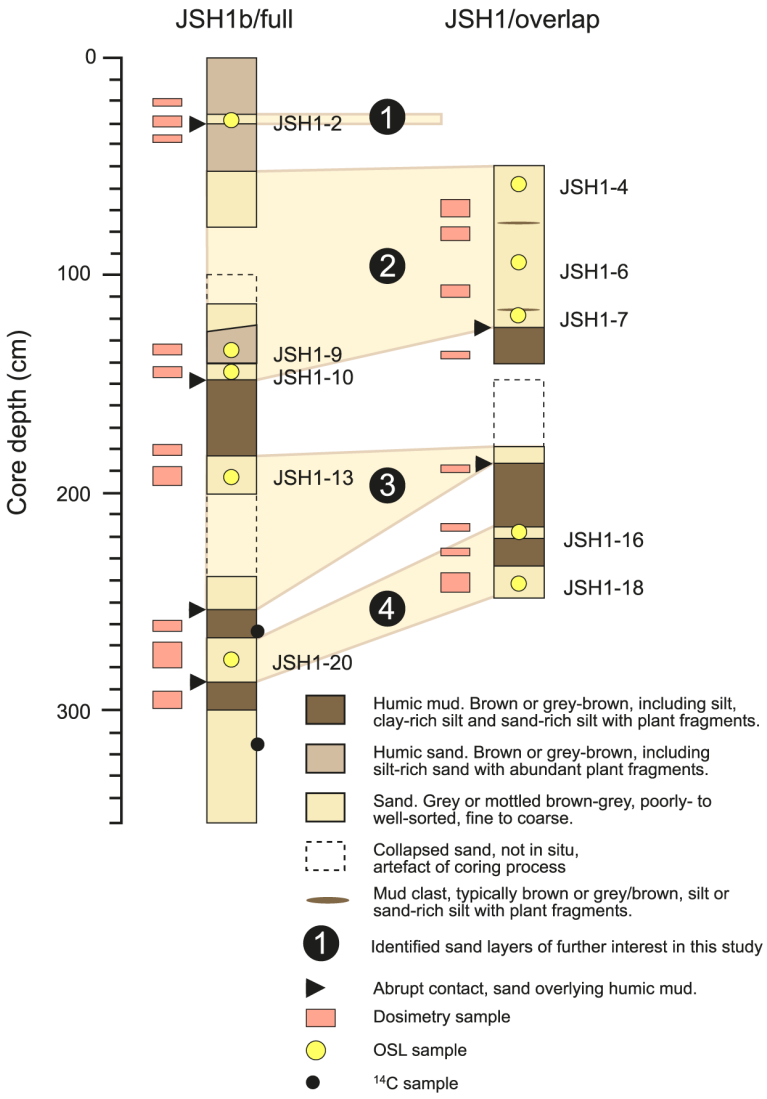

1038
1039

1040 Fig. 3

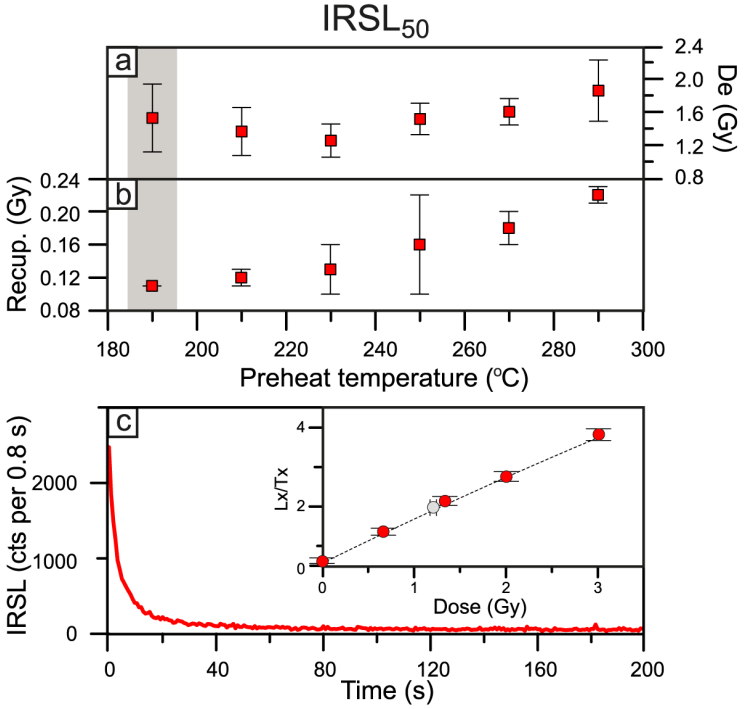

1041
1042

1043 Fig. 4

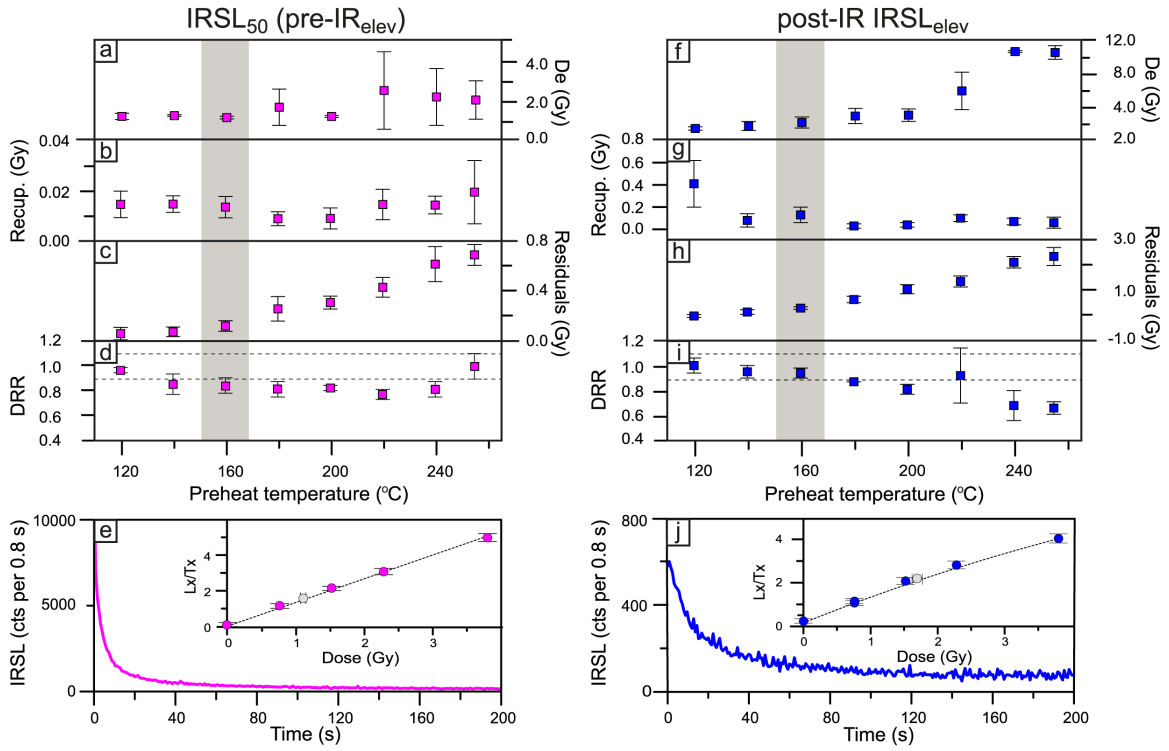

1044
1045
1046 Fig. 5

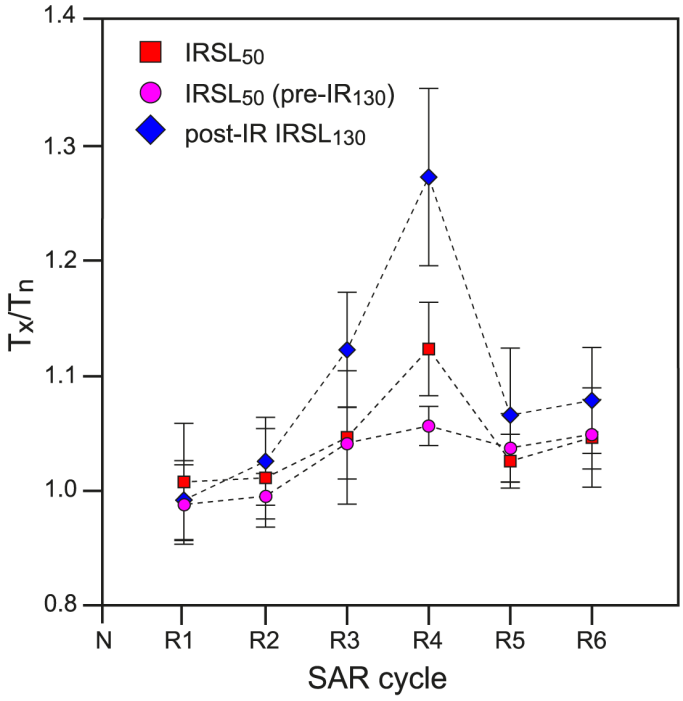

1047
1048
1049

1050 Fig. 6

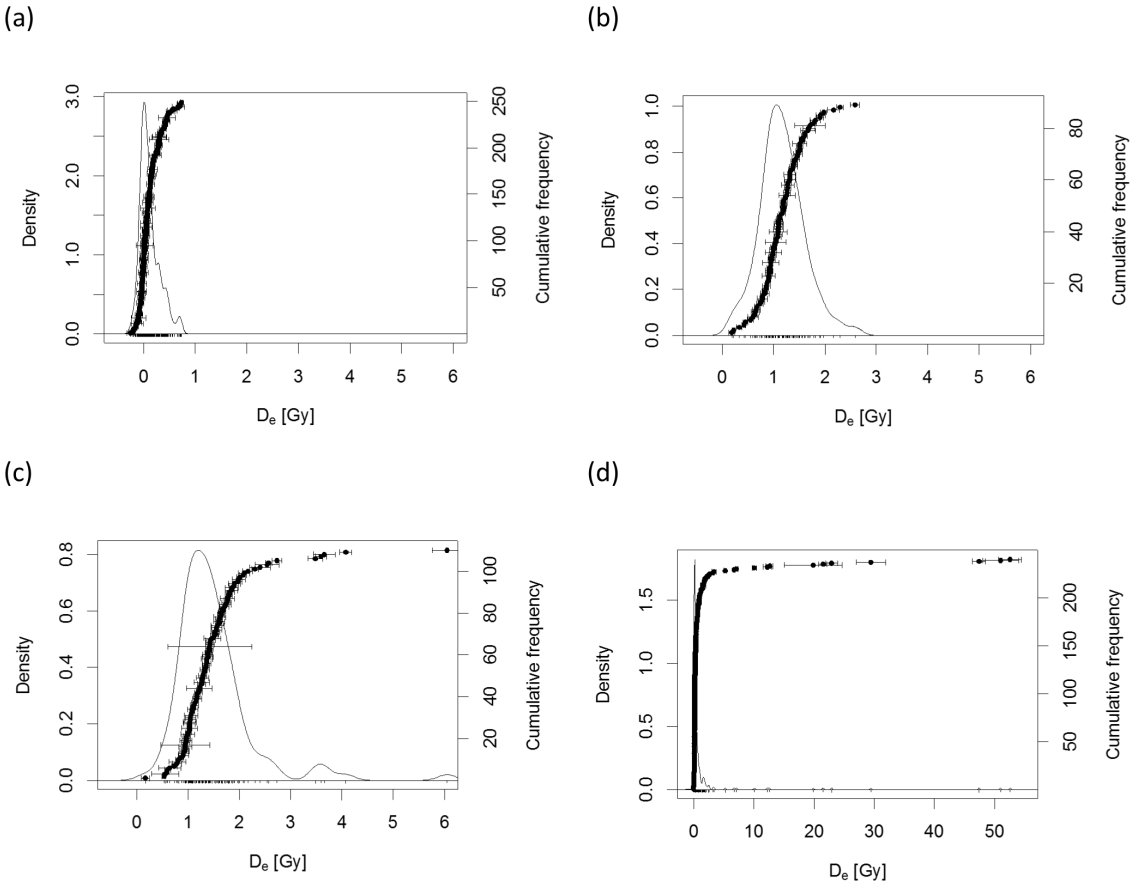

1051
1052
1053 Fig. 7

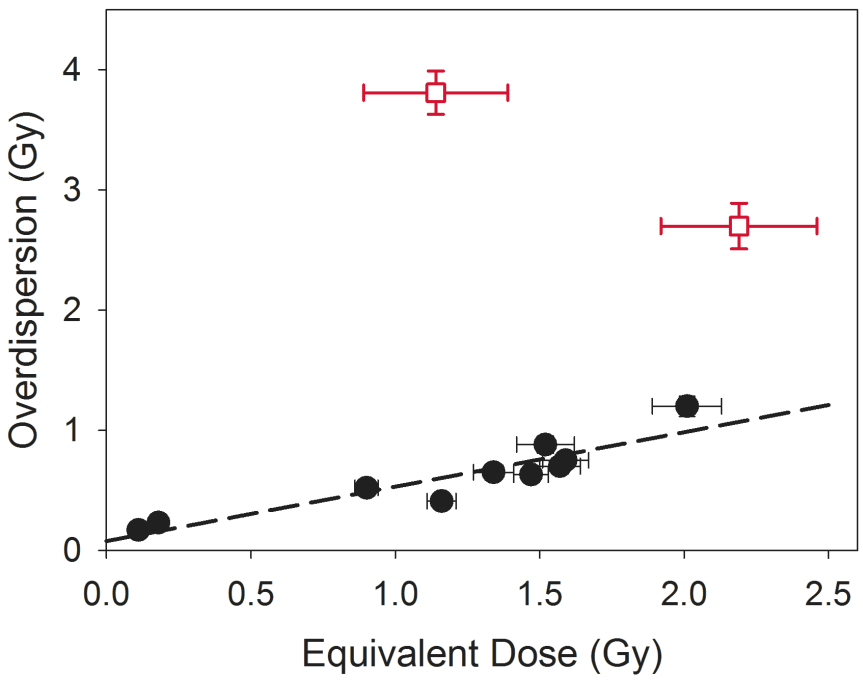

1054
1055

1056 Fig. 8

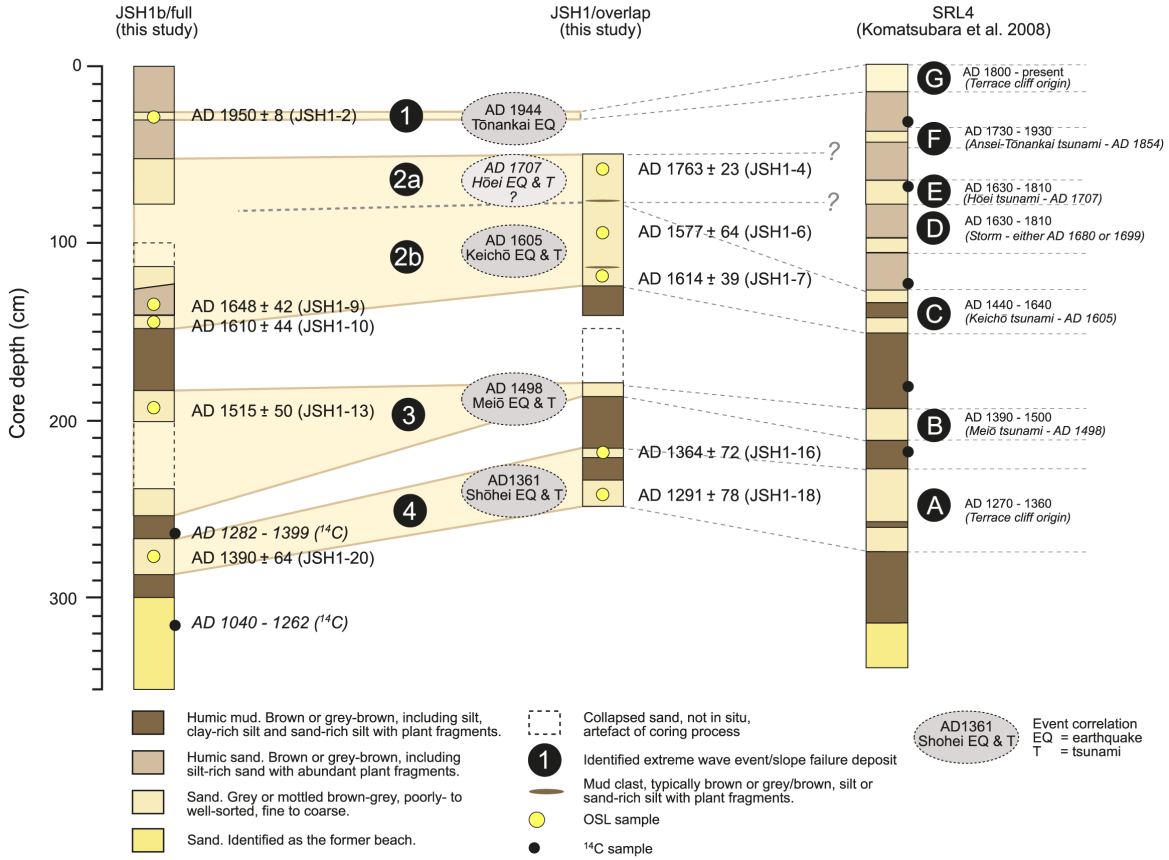

1057
1058

1059 Fig. S1

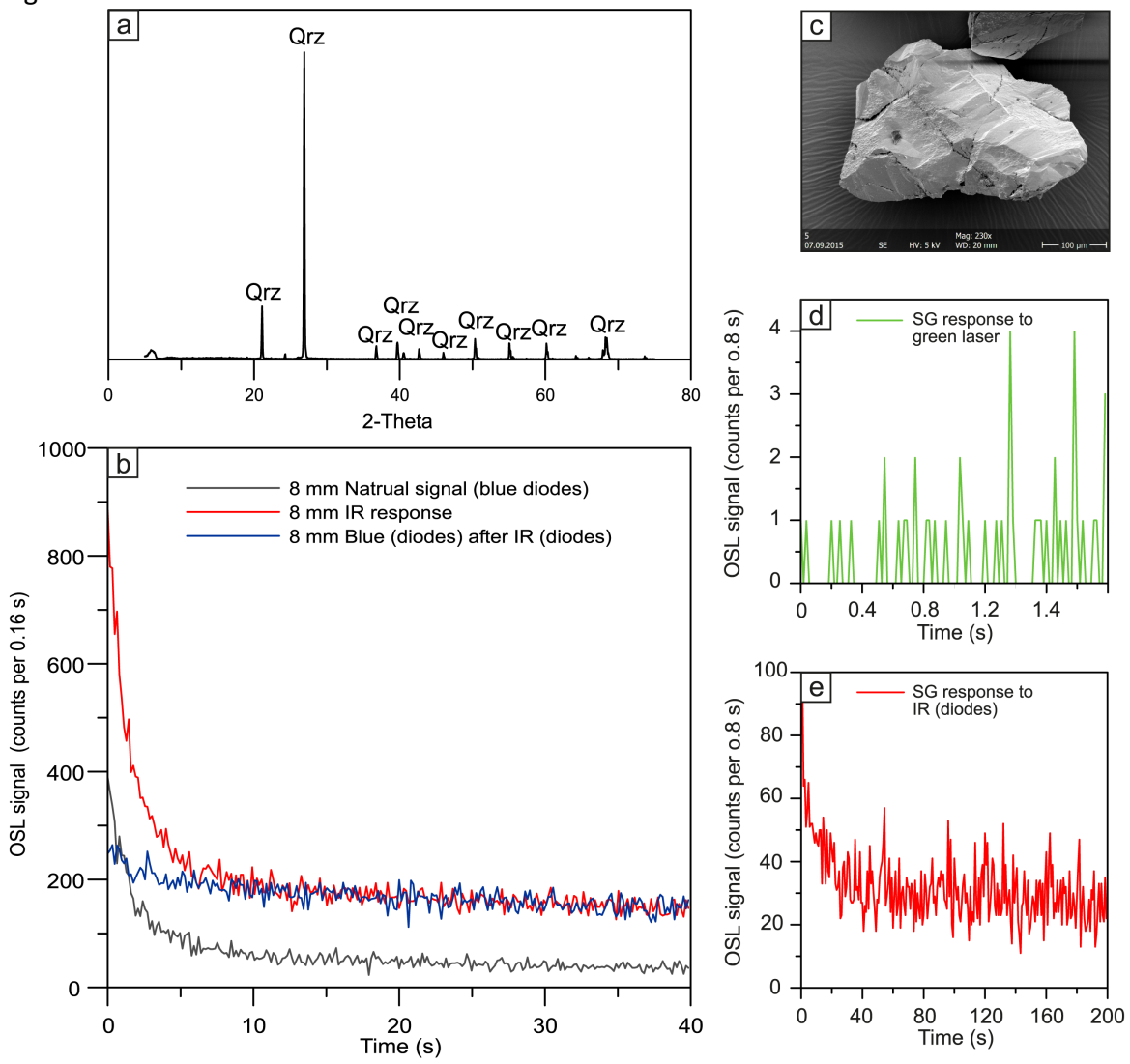

1060
1061

Fig. S2

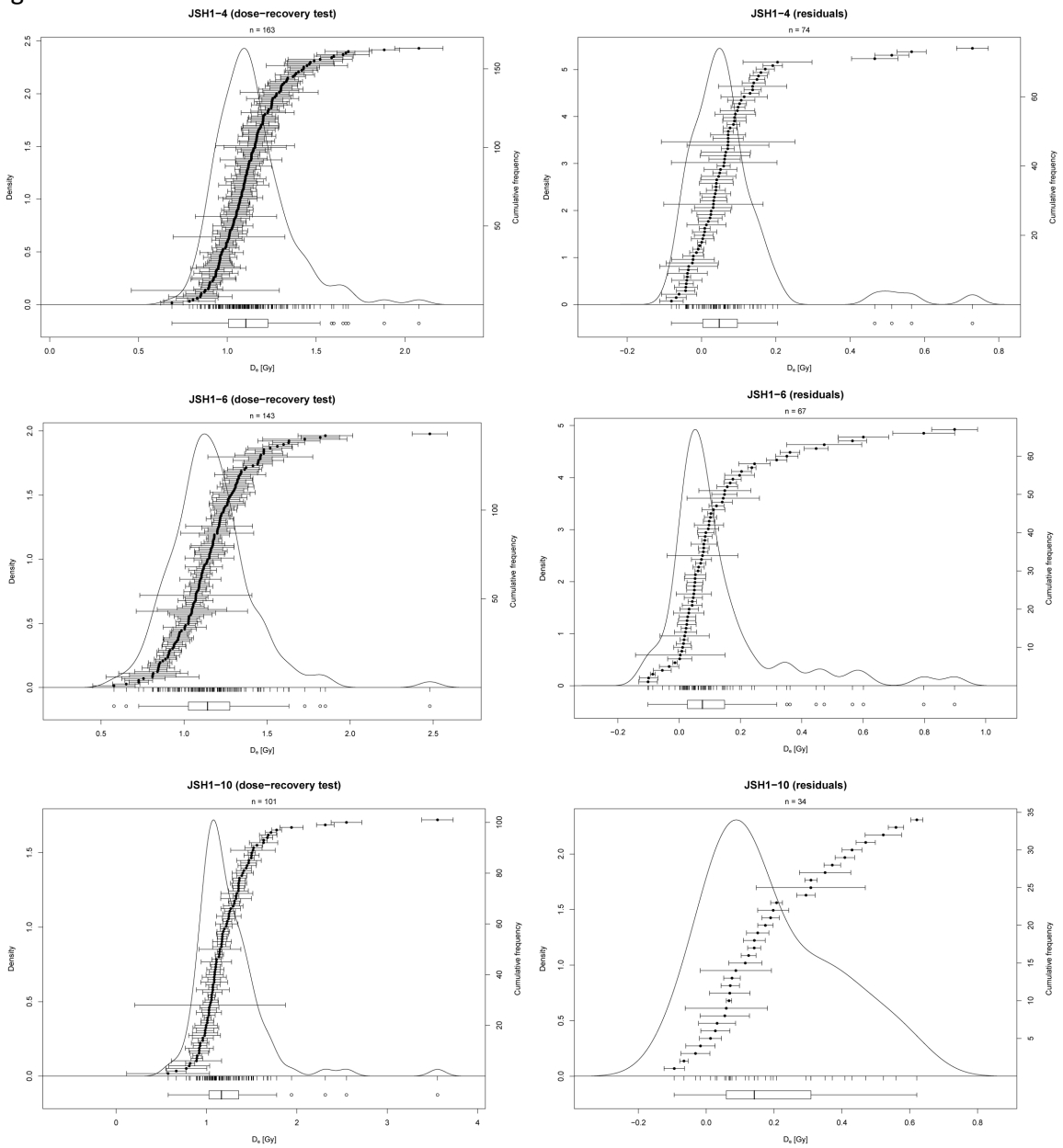
JSH1−4 (dose−recovery test)
n = 163
JSH1−4 (residuals)
n = 74
JSH1−6 (dose−recovery test)
n = 143
JSH1−6 (residuals)
n = 67
JSH1−10 (dose−recovery test)
n = 101
JSH1−10 (residuals)
n = 34
Density
Cumulative frequency
De [Gy]

1065 Fig. S3

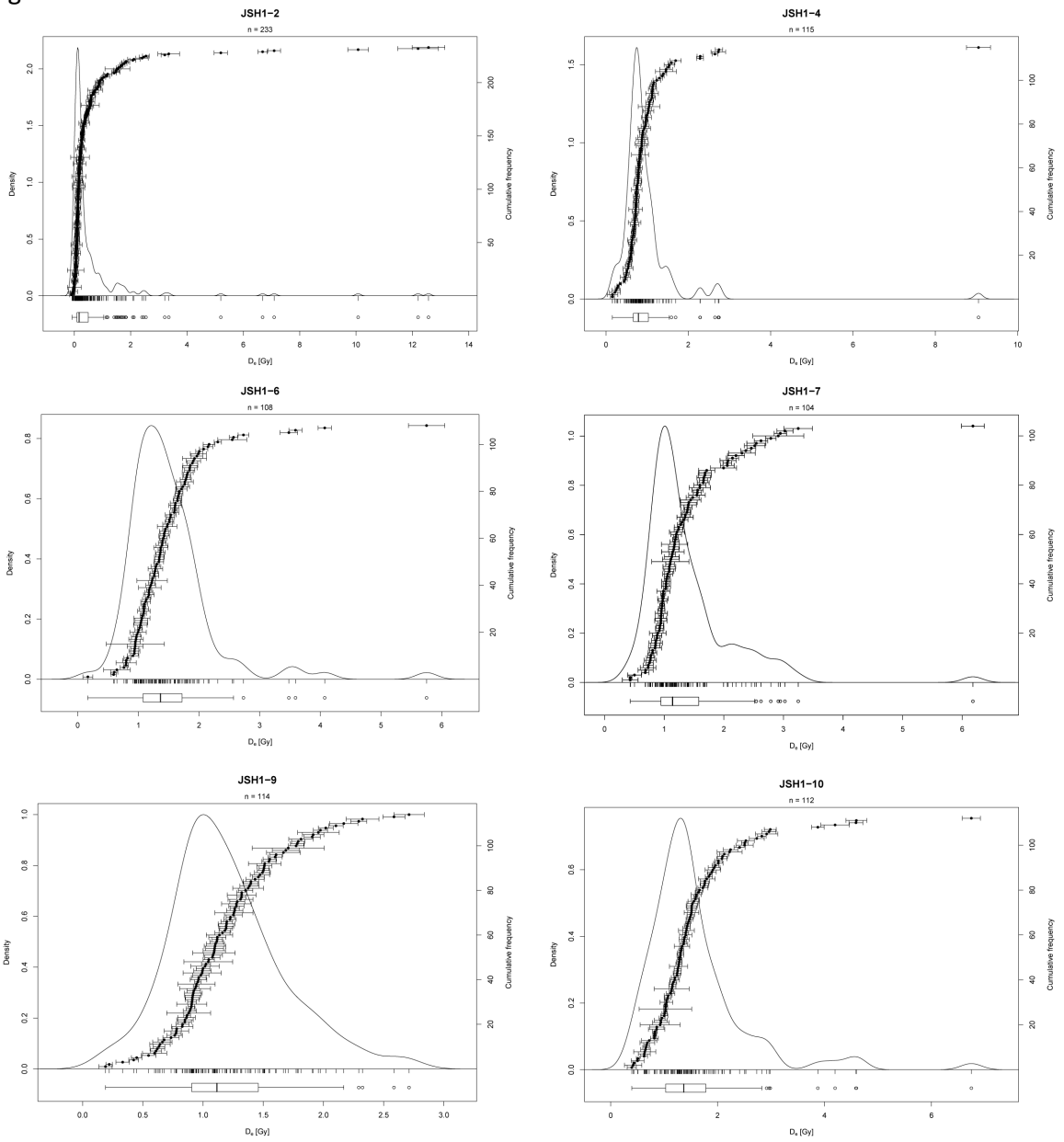

1066
1067

1068 Fig. S4

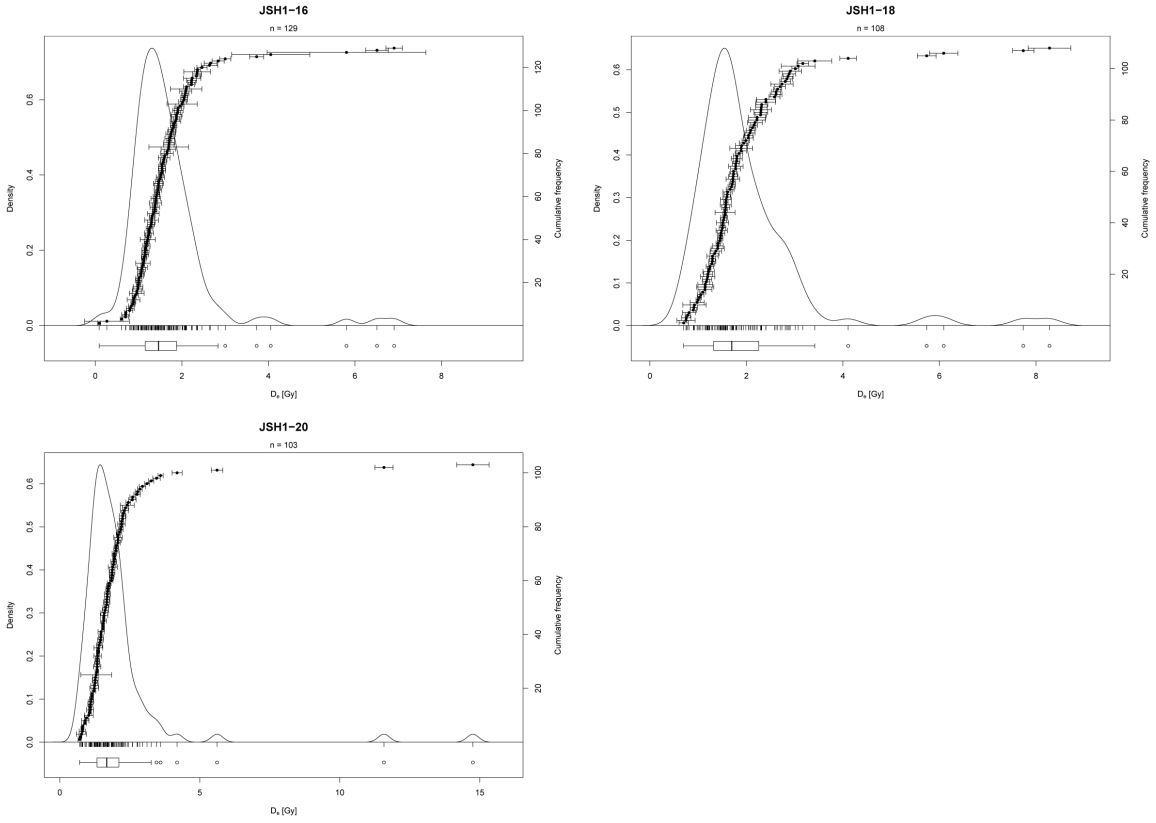

1069